 doi:10.20944/preprints202105.0724.v1

Article

Functionalization of photosensitized silica nanoparticles for advanced photodynamic therapy of cancer

Ruth Prieto-Montero[1§], Alejandro Prieto-Castañeda[2§], Alberto Katsumiti[3,4§], Miren P. Cajaraville[3], Antonia R. Agarrabeitia[2], María J. Ortiz[2*], Virginia Martínez-Martínez[1*]

[1] Departamento de Química Física, Universidad del País Vasco/Euskal Herriko Unibertsitatea (UPV/EHU), 48080 Bilbao, Spain
[2] Departamento de Química Orgánica, Facultad de CC. Químicas, Universidad Complutense de Madrid, 28040 Madrid, Spain
[3] CBET Research Group, Dept. Zoology and Animal Cell Biology; Faculty of Science and Technology and Research Centre for Experimental Marine Biology and Biotechnology PiE, University of the Basque Country UPV/EHU, Basque Country, Spain.
[4] Biotechnology Division, GAIKER Technology Centre, Basque Research and Technology Alliance (BRTA), 48170 Zamudio, Spain.

* Correspondence: mjortiz@quim.ucm.es and virginia.martinez@ehu.eus; Tel.: +34-946-015-969
§ Equally contributed

Abstract: BODIPY dyes have recently raised attention as potential photosensitizers. In this work, commercial and novel photosensitizers (PSs) based on BODIPY chromophores (haloBODIPYs and orthogonal dimers strategically designed with intense bands in the blue, green or red region of the Visible spectra and high singlet oxygen production) were covalently linked to mesoporous silica nanoparticles (MSNs) further functionalized with PEG and folic acid (FA). MSNs of approximately 50 nm in size with different functional groups were synthesized to allow multiple alternatives of PS-PEG-FA decoration of their external surface. Different combinations varying the type of PS (commercial Rose Bengal, Thionine and Chlorine e6 or custom-made BODIPY-based), the linkage design and the length of PEG are detailed. All the nanosystems were physicochemically characterized (morphology, diameter, size distribution and PS loaded amount) and photophysically studied (absorption capacity, fluorescence efficiency, and singlet oxygen production) in suspension. For the most promising PS-PEG-FA silica nanoplatforms, the biocompatibility in dark conditions and the phototoxicity under suitable irradiation wavelengths (blue, green, or red) at regulated light doses (10-15 J/cm^2) were compared with PSs free in solution in HeLa cells *in vitro*.

Keywords: BODIPY-based photosensitizers, functionalized silica nanoparticles, folic acid, PEG, photodynamic therapy; HeLa cells, (photo) toxicity.

1. Introduction

Currently, several alternatives are used to treat cancer such as surgery, chemo-, radio- or immune- therapy, although depending on the type of cancer an effective method has not been found yet. In this regard, Photodynamic Therapy (PDT) is a complementary treatment that can be applied as a combined therapy to enhance the anticancer efficiency by a synergic or additive effect with the conventional methods. PDT involves a light source, a photosensitizer (PS), and oxygen. During PDT, PS is activated under light at a specific wavelength to generate reactive oxygen species (ROS), mainly singlet oxygen ($^1O_2$), a cytotoxic species able to promote apoptosis or necrosis of cancer cells [1]. Nowadays preclinical and clinical trials have proven PDT to be effective in early-stage tumors or the palliation of advanced cancers, such as skin, head, neck, esophageal, or lung cancer, improving patient survival [2–5]. PDT is considered a less invasive and more precise treatment (locally controlled by the light irradiation of malignant tissue), without inducing long-term side effects and it has a lower cost with respect to other treatments.

 doi:10.20944/preprints202105.0724.v1

Nevertheless, the limitations of PDT are mainly related to the availability of the PSs. Despite there are several PSs approved by the FDA, most of them are hydrophobic and/or tend to have poor selectivity to malignant tissues [6–9].

The ideal PS to be used as a photoactive drug for PDT should be non-cytotoxic in dark conditions, selective to cancer tissues, and display limited stability *in vivo* to minimize side effects; should have intense absorption bands ($\varepsilon \geq 50000$ M-1cm-1), preferentially in the phototherapeutic window to ensure deeper penetration of light into tissues [10] (630-850 nm), and high singlet oxygen production to reduce doses and irradiation time; should be photoresistant to avoid the photodecomposition of the PS during treatment, and finally, should present an amphiphilic nature being soluble in water as well as permeable through the cell membrane. At the moment, few PSs fulfill these requirements and new molecular designs are demanded [6,7,11–14]. One approach to obtain new molecules is focused on the synthesis of improved PS to overcome their limitations but this usually requires multistep chemistry increasing the costs and production time, hampering the implementation for clinical uses. In this context, BODIPY dyes have recently raised attention as potential photosensitizers [15–18]. They are characterized by intense absorption and emission bands in the green region and resistance to photobleaching [19,20]. Despite being highly fluorescent chromophores (antagonistic property to ROS generation) and poorly soluble in water, their synthesis allows an easy, versatile, and selective modification of their molecular structure to increase the population of the triplet state and consequently their singlet oxygen generation and also shifts their spectroscopic bands into the clinic window. These modifications include the addition of iodine heavy atoms, π-conjugated systems in the BODIPY skeleton, or the design of orthogonal BODIPY dimers [15,17,18,21–32].

Another alternative is the use of nanomaterials as (photo)drug carriers. They have a large surface to volume ratio which allows the administration of a high amount of active components, preventing their degradation or inactivation by plasma components, delivering soluble and stable formulations in aqueous media, and enhancing their accumulation inside tumor tissues by the so-called passive targeting due to enhanced permeability and retention (EPR) effect [11,33–42]. Besides, the selectivity to cancer cells can be improved by active targeting, through surface modifications with target ligands, such as proteins, polysaccharides, nucleic acids, peptides and small molecules that bind to specific receptors overexpressed on the surface of malignant cells but not on healthy cells [9,43–45].

Currently, there are many different types of nanoparticles based on liposomes, polymeric, micellar, metallic, or protein for medical use [33,35–40,46–48]. Silica nanoparticles (SN) have attracted attention as carriers for drug delivery due to their properties, such as reduced toxicity, good biocompatibility, high surface area, easy functionalization, optical transparency, and low cost [49,50]. PS-loaded silica nanoparticles have been reported as promising singlet oxygen generator platforms, improving the photoactive drug delivery by enhancing PS poor solubility and selectivity for cancer cells [51–55]. The PS can be physically encapsulated or covalently attached to the internal or external surface of the silica nanoparticles [56–60]. Briefly, loading PS within the nanostructure ensures a high photostability but restrains the diffusion of oxygen species (molecular oxygen towards inside and singlet oxygen towards outside). It was demonstrated that nanoparticles with draped-PS outside lead to better $^1O_2$ productivity than PS located inside [61–63].

In this work, different PSs (Figure 1) were tethered to the external surface of 50 nm MSNs. First, three commercially available PSs, Rose Bengal (RB), Chlorin e6 (C6), and Thionine (Th), recognized as suitable singlet oxygen generators and extensively employed in PDT were used [6,9–11,52,64–66]. These dyes already have functional groups in their molecular structure (carboxylic in Rose Bengal and Chlorin e6 and amine in Thionine) and can be easily grafted to the external surface of MSNs. Afterward, seven custom-made BODIPY-based PSs were used, which were rationally designed to effectively generate high singlet oxygen production under illumination at different wavelengths of

Preprints (www.preprints.org) | NOT PEER-REVIEWED | Posted: 31 May 2021 doi:10.20944/preprints202105.0724.v1

the Visible spectra (blue, green or red light) [12,18,24,30,67,68], and to endow suitable graftable groups to be anchored at MSNs.

Additionally, MSNs were externally coated with polyethylene glycol (PEG) as it is usually required to stabilize nanoparticle systems, enhance their life-time in the blood system and avoid the induction of immune responses [34,38,41,69–73]. For that, several PEG derivatives (Figure 1) with different graftable groups at one end of the chain (succinimide group or with silyl group Si-PEG) were tethered at the MSN shell. The length of the polymer chain (750 Da, 2000 Da, and 5000 Da) was also adjusted to improve nanoparticle stabilization in water.

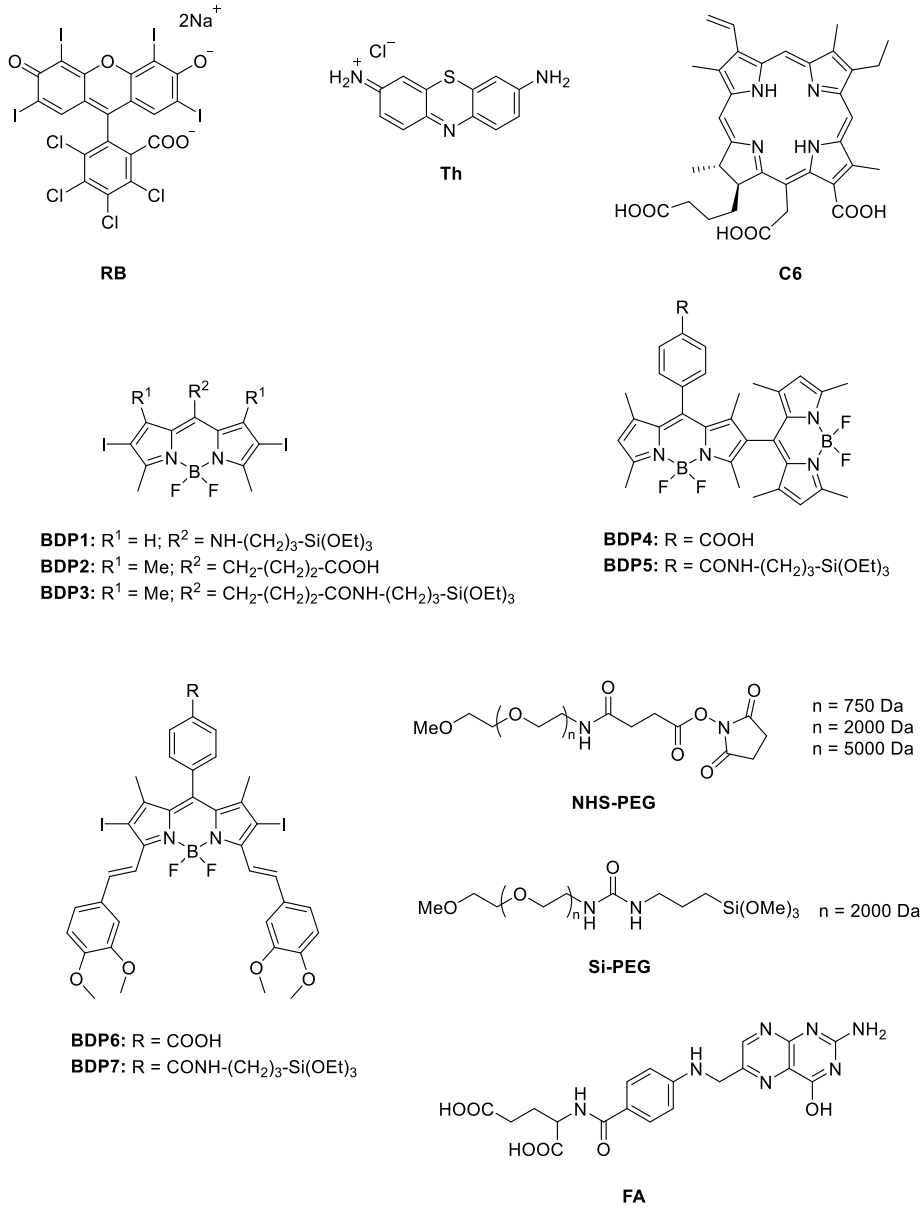

Figure 1. Molecular structure of the different compounds anchored to MSN: commercial (RB, Th, C6) and custom-made BODIPY photosensitizers (BDP1-BDP7), PEG derivatives with different functional groups (Si-PEG and NHS-PEG) and molecular weight (750 Da, 2000 Da and 5000 Da) and FA.

Finally, the selectivity of MSNs for cancer cells was enhanced by the addition of a peripheral target for cancer cells. Folic acid (FA), a low cost, stable and small molecule with available functional groups (Figure 1), is widely used to target several types of cancer cells, in particular, those overexpressing folate receptors (FR) on their surface,

Preprints (www.preprints.org) | NOT PEER-REVIEWED | Posted: 31 May 2021 doi:10.20944/preprints202105.0724.v1

such as ovarian, endometrial and kidney cancer cells [74,75]. Thus, tethering FA on nanoparticle's surface promotes a higher cellular uptake via endocytosis [76–79]. In fact, our recently published study has quantitatively demonstrated a significantly higher accumulation of FA-functionalized fluorescent MSNs compared to nanoparticles without FA in HeLa cells [80].

The linkage between the PSs and the MSNs and the length of PEG were firstly optimized with the commercial PS Rose Bengal and then implemented for the rest of PSs. The physicochemical features (morphology, diameter, size distribution, PS loaded amount) and photophysical properties (absorption capacity, fluorescence efficiency, and singlet oxygen production) were detailed. The efficiency of the PS-PEG-FA MSN nanoplatforms was tested in HeLa cells *in vitro* and the results were compared with those obtained in cells exposed to PSs free in solution.

2. Materials and Methods

2.1. Materials and Methods

All starting materials and reagents for the MSNs synthesis were used as commercially provided unless otherwise indicated. Tetraethoxysilane (TEOS) (≥99%), ammonium hydroxide solution (NH_4OH) (25% NH_3 basis), hexadecyltrimethylammonium bromide (CTAB) (≥98%), 3-aminopropyltrimethoxysilane (APTMS) (97%), 3-cyanopropyltriethoxysilane (CTES) (98%), 3-aminopropyltriethoxysilane (APTES) (99%), 1-hydroxybenzotriazole hydrate (HOBt) (≥97%), boron trifluoride diethyl etherate (for synthesis), dimethylformamide anhydrous (DMF) (99.8%), 3,4-dimethoxybenzaldehyde (99%), piperidine (≥99.5%), 2,3-dichloro-5,6-dicyano-1,4-benzoquinone (DDQ) (98%), *N*-hydroxysuccimide (NHS) (98%), *N*-(3-(dimethylaminopropyl)-*N'*-ethylcarbodiimide (EDC) (≥97%), triethylamine (TEA) (≥99%) and folic acid (FA) (≥97%) were purchased from Sigma-Aldrich; Ethyl chloroformate (≥99%) and 2,4-dimethylpyrrole (97%) were supplied from Acros; trifluoroacetic acid (TFA) (99%) was purchased from Alfa Aesar; acetic acid glacial (synthesis grade) from Scharlab; polyethylene glycol (Si-PEG) (2000 Da, >95%) from Iris BIOTECH GMBH (Maktredwitz, Germany); NHS-PEG derivative (750 Da (>95%) and 2000 Da (>95%), supplied by Iris BIOTECH GMBH, and 5000 Da (≥80%) by Sigma-Aldrich.

2.2. Synthesis of new BODIPY based PSs

2.2.1. General

Anhydrous solvents were prepared by distillation over standard drying agents according to common methods. All other solvents were of HPLC grade and were used as provided. Flash chromatography was performed using silica gel (230-400 mesh). NMR spectra were recorded using $CDCl_3$ or $CDCl_3/CD_3OD$ at 20 ºC. ^1H NMR and ^{13}C NMR chemical shifts (δ) were referenced to internal solvent $CDCl_3$ (δ = 7.260 and 77.03 ppm, respectively) or CD_3OD (δ = 3.205/4.031 and 52.69 ppm, respectively). Multiplicity is indicated as follows: s = singlet; d = doublet; dd = double doublet; t = triplet; q = quadruplet; quint = quintuplet; m = multiplet. Coupling constants (*J*) are dated in hertz (Hz). DEPT 135 experiments were used to determine the type of carbon nucleus (C *vs*. CH *vs*. CH_2 *vs*. CH_3). FTIR spectra were obtained from neat samples using the attenuated total reflection (ATR) technique. High-resolution mass spectrometry (HRMS) was performed using electronic impact (EI) or MALDI-TOF and ion trap (positive mode) for the detection.

BDP1 [81]**, BDP2** [82], 8-(4-carboxyphenyl)-2-formyl-1,3,5,7-tetramethylBODIPY [83] and 8-(4-carboxyphenyl)-2,6-diiodo-1,3,5,7-tetramethylBODIPY [84] were synthesized by the corresponding described methods. The synthesis of BODIPYs **BDP3-BDP7** is illustrated in Scheme S1 (see supporting information).

2.2.2. General procedure for the formation of amides

The corresponding carboxy-BODIPY (1 mol. equiv.), APTES (2.1 mol. equiv), TEA (2 mol. equiv.), EDC (2 mol. equiv.) and HOBt (2 mol. equiv.) were dissolved in CH_2Cl_2 and

Preprints (www.preprints.org) | NOT PEER-REVIEWED | Posted: 31 May 2021 doi:10.20944/preprints202105.0724.v1

stirred under argon at rt for 12 h. The reaction mixture was then washed with HCl 10% and water. The obtained organic layer was dried over anhydrous Na_2SO_4, filtered and the solvent evaporated to dryness. The obtained residue was submitted to purification by flash chromatography on silica gel.

2.2.3. Synthesis of **BDP3**

According to the general procedure described in section 2.2.2., **BDP2** [82] (70 mg, 0.12 mmol), APTES (0.06 mL, 0.25 mmol), TEA (0.03 mL, 0.24 mmol), EDC (46 mg, 0.24 mmol) and HOBt (32 mg, 0.24 mmol) in CH_2Cl_2 (10 mL) were reacted. Flash chromatography (CH_2Cl_2/EtOAc, 90:10) afforded **BDP3** (39 mg, 41%) as an orange-red solid. ^{1}H NMR (300 MHz, $CDCl_3$) δ 5.84 (t, J = 5.4 Hz, 1H, NH), 3.82 (q, J = 6.9 Hz, 6H, $3CH_2O$), 3.26 (q, J = 6.9 Hz, 2H, CH_2N), 3.11-3.05 (m, 2H, CH_2), 2.61 (s, 6H, $2CH_3$), 2.49 (s, 6H, $2CH_3$), 2.32 (t, J = 6.9 Hz, 2H, CH_2), 1.99-1.90 (m, 2H, CH_2), 1.64 (quint, J = 7.8 Hz, 2H, CH_2), 1.22 (t, J = 6.9 Hz, 9H, $3CH_3$), 0.64 (t, J = 7.8 Hz, 2H, CH_2Si) ppm. ^{13}C NMR (75 MHz, $CDCl_3$) δ 171.1 (CONH), 155.5 (C), 145.3 (C), 142.5 (C), 131.5 (C), 86.6 (C-I), 58.5 (CH_2), 41.9 (CH_2), 36.1 (CH_2), 28.4 (CH_2), 27.3 (CH_2), 22.9 (CH_2), 19.0 (CH_3), 18.3 (CH_3), 16.2 (CH_3), 7.9 (CH_2) ppm. FTIR ν 3302, 2971, 2924, 1712, 1620, 1542, 1463, 1392, 1346, 1190, 1084, 1003, 958 cm^{-1}. HRMS-EI m/z 789.0931 (calcd. for $C_{26}H_{40}BF_2I_2N_3O_4Si$: 789.0939).

2.2.4. Synthesis of **BDP4**

To a degassed solution of 8-(4-carboxyphenyl)-2-formyl-1,3,5,7-tetramethylBODIPY [83] (186 mg, 0.47 mmol) in dry CH_2Cl_2 (15 mL) were added a solution of 2,4-dimethylpyrrole (0.10 mL, 0.98 mmol) in dry CH_2Cl_2 (2 mL) and two drops of TFA, and the resulting mixture stirred at rt for 2 h. After, a solution of DDQ (117.0 mg, 0.51 mmol) in CH_2Cl_2 (10 mL) was added, and the resulting new mixture stirred for 30 min. Then, TEA (0.32 mL, 2.34 mmol) and BF_3 Et_2O (0.58 mL, 4.68 mmol) were added to the mixture, and the resulting final mixture stirred for 3 h at rt, washed with HCl 10%, and water. The obtained organic layer was dried over anhydrous Na_2SO_4, filtered and the solvent evaporated to dryness. Flash chromatography (CH_2Cl_2/EtOAc, 30:70) afforded **BDP4** (78 mg, 27%) as an orange solid. ^{1}H NMR (300 MHz, $CDCl_3$) δ 8.27 (d, J = 8.1 Hz, 2H, 2CH), 7.46 (d, J = 8.1 Hz, 2H, 2CH), 6.10 (s, 1H, CH), 5.99 (s, 2H, 2CH), 2.61 (s, 3H, CH_3), 2.52 (s, 6H, $2CH_3$), 2.42 (s, 3H, CH_3), 1.71 (s, 6H, $2CH_3$), 1.41 (s, 3H, CH_3), 1.21 (s, 3H, CH_3) ppm. ^{13}C NMR (75 MHz, $CDCl_3$) δ 170.6 (COOH), 159.4 (C), 155.9 (C), 151.3 (C), 145.2 (C), 142.3 (C), 140.7 (C), 140.2 (C), 138.0 (C), 133.2 (C), 132.0 (C), 131.8 (C), 131.2 (CH), 130.4 (C), 130.3 (C), 128.4 (CH), 126.0 (C), 122.9 (CH), 121.3 (CH), 14.9 (CH_3), 14.8 (CH_3), 14.6 (CH_3), 14.0 (CH_3), 12.8 (CH_3), 12.3 (CH_3) ppm. FTIR ν 2924, 2855, 1709, 1546, 1464, 1311, 1193, 1078, 981 cm^{-1}. HRMS-EI m/z 614.2636 (calcd. for $C_{33}H_{32}B_2F_4N_4O_2$: 614.2648).

2.2.5. Synthesis of **BDP5**

According to the general procedure described in section 2.2.2., **BDP4** (46 mg, 0.07 mmol), APTES (0.04 mL, 0.15 mmol), TEA (0.02 mL, 0.14 mmol), EDC (28 mg, 0.14 mmol) and HOBt (20 mg, 0.15 mmol) in CH_2Cl_2 (10 mL) were reacted. Flash chromatography (hexane/EtOAc, 60:40) afforded **BDP5** (30 mg, 49%) as an orange solid. ^{1}H NMR (300 MHz, $CDCl_3$) δ 7.95 (d, J = 8.1 Hz, 2H, 2CH), 7.39 (d, J = 8.1 Hz, 2H, 2CH), 6.71 (t, J = 5.4 Hz, 1H, NH), 6.08 (s, 1H, CH), 5.98 (s, 2H, 2CH), 3.82 (q, J = 6.9 Hz, 6H, $3CH_2O$), 3.50 (q, J = 6.0 Hz, 2H, CH_2N), 2.60 (s, 3H, CH_3), 2.52 (s, 6H, $2CH_3$), 2.41 (s, 3H, CH_3), 1.79 (quint, J = 7.8 Hz, 2H, CH_2), 1.70 (s, 6H, $2CH_3$), 1.39 (s, 3H, CH_3), 1.21 (t, J = 6.9 Hz, 9H, $3CH_3$), 1.20 (s, 3H, CH_3), 0.73 (t, J = 7.8 Hz, 2H, CH_2Si) ppm. ^{13}C NMR (75 MHz, $CDCl_3$) δ 166.3 (CONH), 159.2 (C), 155.8 (C), 151.1 (C), 145.3 (C), 142.3 (C), 141.1 (C), 138.1 (C), 137.6 (C), 135.8 (C), 133.3 (C), 132.2 (C), 131.8 (C), 130.5 (C), 128.2 (CH), 128.1 (CH), 125.9 (C), 122.8 (CH), 121.3 (CH), 58.6 (CH_2O), 42.4 (CH_2), 22.8 (CH_2), 18.3 (CH_3), 14.83 (CH_3), 14.80 (CH_3), 14.6 (CH_3), 13.9 (CH_3), 12.8 (CH_3), 12.3 (CH_3), 8.0 (CH_2) ppm. FTIR ν 2924, 2854, 1646, 1546, 1513, 1310, 1193, 1078, 980 cm^{-1}. HRMS-MALDI-TOF m/z 817.3979 (calcd. for $C_{42}H_{53}B_2F_4N_5O_4Si$: 817.3989).

2.2.6. Synthesis of **BDP6**

Preprints (www.preprints.org) | NOT PEER-REVIEWED | Posted: 31 May 2021 doi:10.20944/preprints202105.0724.v1

8-(4-Carboxyphenyl)-2,6-diiodo-1,3,5,7-tetramethylBODIPY [84] (25 mg, 0.04 mmol) in DMF (2 mL), 3,4-dimethoxybenzaldehyde (20 mg, 0.12 mmol), piperidine (0.02 mL, 0.20 mmol) and acetic acid (0.01 mL, 0.20 mmol) were added to a microwave tube. The tube was sealed with an aluminum cap and heated for 20 min at 80 ºC under microwave radiation (Biotage® Initiator Classic). After cooled down to rt, CH_2Cl_2 was added and the organic layer washed with water, dried over anhydrous Na_2SO_4, filtered, and evaporated to dryness. The obtained residue was submitted to purification by flash chromatography on silica gel with EtOAc/CH_3OH (95:5) to give **BDP6** (16 mg, 43%) as a green solid. ^{1}H NMR (700 MHz, $CDCl_3$/CD_3OD 4:1) δ 8.09 (d, J = 8.4 Hz, 2H, 2CH), 7.98 (d, J = 16.8 Hz, 2H, 2CH=C), 7.42 (d, J = 16.8 Hz, 2H, 2C=CH), 7.30 (d, J = 8.4 Hz, 2H, 2CH), 7.09 (dd, J = 8.4 and 2.1 Hz, 2H, 2CH), 7.04 (d, J = 2.1 Hz, 2H, 2CH), 6.78 (d, J = 8.4 Hz, 2H, 2CH), 3.82 (s, 6H, 2CH_3O), 3.79 (s, 6H, 2CH_3O), 1.31 (s, 6H, 2CH_3) ppm. ^{13}C NMR (176 MHz, $CDCl_3$/CD_3OD 4:1) δ 172.0 (COOH), 154.7 (C), 154.4 (C), 153.1 (C), 149.5 (C), 143.7 (C), 143.6 (CH), 143.5 (CH), 141.1 (C), 136.4 (C), 135.9 (C), 134.8 (CH), 134.7 (CH), 133.8 (C), 132.7 (CH), 132.6 (CH), 125.8 (CH), 120.7 (CH), 115.2 (CH), 115.1 (CH), 113.7 (CH), 87.1 (C-I), 59.82 (CH_3O), 59.78 (CH_3O), 21.5 (CH_3) ppm. FTIR ν 2924, 2852, 1694, 1591, 1514, 1461, 1265, 1176, 1101, 1012 cm^{-1}. HRMS-MALDI-TOF m/z 906.0638 (calcd. for $C_{37}H_{35}BF_2I_2N_2O_6$: 906.0646).

2.2.7. Synthesis of **BDP7**

According to the general procedure described in section 2.2.2., **BDP6** (37 mg, 0.04 mmol), APTES (0.02 mL, 0.085 mmol), TEA (0.01 mL, 0.08 mmol), EDC (15 mg, 0.08 mmol) and HOBt (11 mg, 0.08 mmol) in CH_2Cl_2 (10 mL) were reacted for 12 h. Flash chromatography (CH_2Cl_2/EtOAc, 90:10) afforded **BDP7** (14 mg, 32%) as a red solid. ^{1}H NMR (700 MHz, $CDCl_3$) δ 8.12 (d, J = 16.8 Hz, 2H, 2CH=C), 7.99 (d, J = 8.4 Hz, 2H, 2CH), 7.57 (d, J = 16.8 Hz, 2H, 2C=CH), 7.41 (d, J = 8.4 Hz, 2H, 2CH), 7.23 (dd, J = 8.4 and 1.4 Hz, 2H, 2CH), 7.16 (d, J = 1.4 Hz, 2H, 2CH), 6.90 (d, J = 8.4 Hz, 2H, 2CH), 6.79 (t, J = 6.3 Hz, 1H, NH), 3.96 (s, 6H, 2CH_3O), 3.93 (s, 6H, 2CH_3O), 3.86 (q, J = 7.0 Hz, 6H, 3CH_2O), 3.54 (q, J = 6.3 Hz, 2H, CH_2N), 1.85-1.80 (m, 2H, CH_2), 1.43 (s, 6H, 2CH_3), 1.24 (t, J = 7.0 Hz, 9H, 3CH_3), 0.77 (t, J = 7.7 Hz, 2H, CH_2Si) ppm. ^{13}C NMR (176 MHz, $CDCl_3$) δ 166.4 (CONH), 150.7 (C), 150.5 (C), 149.2 (C), 145.4 (C), 139.6 (CH), 138.4 (C), 137.0 (C), 135.9 (C), 132.6 (C), 129.8 (C), 128.8 (CH), 128.1 (CH), 121.9 (CH), 116.9 (CH), 111.1 (CH), 109.7 (CH), 83.3 (C-I), 58.6 (CH_2O), 56.1 (CH_3O), 56.0 (CH_3O), 42.4 (CH_2), 22.8 (CH_2), 18.4 (CH_3), 17.8 (CH_3), 8.0 (CH_2) ppm. FTIR ν 3487, 2921, 2852, 1743, 1514, 1463, 1176, 1099, 1014 cm^{-1}. HRMS-MALDI-TOF m/z 1119.1824 (calcd. for $C_{47}H_{54}BF_2I_2N_3O_8Si$: 1119.1831).

2.3. Synthesis of the MSNs

The synthesis of mesoporous silica nanoparticles with amine groups at the external surface (NH-MSNs) has been described previously [80,81]. The synthesis route of mesoporous silica nanoparticles with carboxylic group (COOH-MSN) is similar to that described for NH-MSN but in the second step CTES (0.007 mmol) is added instead of APTMS to provide cyane groups at the external surface. After collecting, CN-MSNs were re-suspended in acid solution (H_2O:H_2SO_4 50:50 v/v) and stirring under 140 ºC for 12 h to convert the CN into COOH groups. Then, the sample was cooled down to rt and kept stirring for another 24 h. Finally, the COOH-MSNs were washed several times with water, until collecting neutral supernatants, Figures S1-S3.

2.4. Grafting of Molecules (PS, PEG and FA) on MSN Surface

The different functionalized MSNs varying PS, PEG and FA (Figure 1) and the linkage approach are synthesized and named as follows:

- RB-PEG-NP-**a**: RB (0.03 mmol), previously silylated with an equimolar ratio of APTMS (0.03 mmol) in 20 mL of CH_3CN under stirring for 1 h under inert atmosphere [81], was directly coupled to the structural hydroxyl groups of MSN (40 mg) added afterward. The reaction was kept for 3 h and the nanoparticles were collected by filtration. Then, RB-MSNs were re-suspended in 20 mL of CH_3CN and

Preprints (www.preprints.org) | NOT PEER-REVIEWED | Posted: 31 May 2021 doi:10.20944/preprints202105.0724.v1

then, NHS ester-activated PEG (0.03 mmol), NHS-PEG (Figure 1) was added to react for 3 h with the external primary amine group of NH-MSN to yield stable amide bonds and releasing *N*-hydroxysuccinimide group (NHS). In this type of MSN, the pelygation procedure of the external surface was carried out with three different PEG chains of 750, 2000, and 5000 Da. The corresponding samples were named RB-PEG$_{750}$-NP-**a**, RB-PEG$_{2000}$-NP-**a** and RB-PEG$_{5000}$-NP-**a**, respectively.

- RB-PEG-NP-**b**: RB was linked through its carboxylic group to the amine groups of NH-MSN (40 mg) by carbodiimide method. This method was previously described [80,81]. Briefly, NHS/EDC is added to RB in solution (0.03 mmol in 20 mL of CH_3CN) in equimolar concentration and stirring for 1 h in an inert atmosphere. Then NH-MSN (40 mg) was directly added to the reaction mixture and kept stirring for 3 h, and nanoparticles were collected. In a second step, PEG (0.03 mmol) with a silylated group at one edge (Si-PEG, Figure 1) was externally anchored to the inherent hydroxyl groups of RB-MSN (40 mg), by direct condensation reaction during 3 h.
- RB-PEG-NP-**c**: both RB (0.03 mmol), previously silylated according to the process previously described in sample RB-PEG-NP-**a**, and Si-PEG (0.03 mmol) were simultaneously bound in CH_3CN to the external hydroxyl groups of MSN (40 mg) following the procedure previously mentioned.
- RB-NP-**d**: FA (0.03 mg) was added to RB-PEG-NP-**c** (40 mg), previously re-suspended in CH_3CN (20 mL), and is linked to the amine groups of RB-PEG-NP-**c** sample through the carbodiimide method cited above.

For the rest of the PDT-nanosystems, denoted as *PS*-NP being PS the short name of every PS (indicated in Figure 1), the linkage between PS and MSN is ruled out by the main functional group at the PS (Figure 1). That is, the amine group of Th dye is covalently linked to the carboxylic groups of COOH-MSN (previously treated with NHS/EDC). Photosensitizers with silylated groups (BDP1, BDP3, BDP5 and BDP7), were directly coupled to the hydroxyl groups of OH-MSN. Finally, PSs with carboxylic groups (C6, BDP2, BDP4, and BDP6) were grafted to the external amine groups of nanoparticles (NH-MSNs). Note here that, C6 was linked by the previous carbodiimide methods but BODIPYs (BDP2, BDP4, and BDP6) do not withstand such conditions and an alternative synthetic route was performed. BODIPY-COOH was dissolved in CH_3CN anhydride (20 mL) at 0 ºC, ethyl chloroformate and triethylamine were added dropwise in equimolar concentration (0.03 mmol) and the system was kept under vigorously stirring for 30 minutes. Then, NH-MSNs were added at rt and stirred for other 30 min. Finally, the functionalized nanoparticles were washed with EtOH until a colorless supernatant was obtained.

In all these samples, Si-PEG (2000 Da) is tethered at the hydroxyl groups and FA to the amine groups of MSNs. The exception was for Th-MSN in which FA was linked to carboxyl groups, by a previous chemical modification of FA, according to Scheme S2 and Figures S4-S5 [76]. Briefly, the terminal COOH group of FA was modified with *N*-Boc-1,6-hexanediamine (Boc-HDA) and the amine group (FA-HDA) is obtained after removing Boc group, according to the reference [76]. The relative quantity of PS, PEG and FA added to the reaction per mg of nanoparticles was the equivalent for all PS-MSN samples.

2.5. Physicochemical and Photophysical Characterization

The size, shape and morphology of the silica nanoparticles were characterized by electron microscopes, scanning electron microscopy (SEM) and transmission electron microscopy (TEM). SEM images were obtained in a JEOL JSM-6400 (JEOL, Tokyo, Japan) and TEM images were obtained in a Philips SuperTwin CM200 (Thermo Fisher Scientific, Eindhoven, Netherlands) at 200 kV. The nanoparticles size distribution was analyzed by Images-J software (1.52u, National Institute of Health, Bethesda, MD, USA). Dynamic light scattering (DLS) and Zeta potential (Zpot) measurements to analyze the NP size and their stability in suspension were carried out using a Malvern Zetasizer Nano ZS (Mal-

Preprints (www.preprints.org) | NOT PEER-REVIEWED | Posted: 31 May 2021 doi:10.20944/preprints202105.0724.v1

vern Products, Madrid, Spain), which has an Helio-Neon laser (λ = 633 nm). FTIR spectra were obtained from neat samples in powder using ATR technique in Anity-1S Shimadzu spectrometer (Izasa Scientific, Barcelona, Spain) (4000–400 cm^{-1} range) and XPS spectra were recorded by SPECS system (Berlin, Germany) with a Phoibos 150 1D-DLD analyzer and Al Kα (1486.7 eV) as monochromatic radiation.

The absorption spectra were recorded by UV-Vis-NIR Spectroscopy (model Cary 7000, Agilent Technologies, Madrid, Spain) equipped with two lamps (halogen lamp for Vis-IR region and deuterium lamp for UV region). In the case of the silica nanoparticle samples an integrating sphere (model Internal DRA 900, Livingston, UK) was used to reduce the scatter of the samples. The fluorescence measurements were recorded with an Edinburgh Instruments Spectrofluorimeter (FLSP920 model, Livingston, UK) equipped with a xenon flash lamp 450 W as the excitation source. The fluorescence spectra were corrected from the wavelength dependence on the detector sensibility.

The fluorescence quantum yields of the photosensitizers were measured by relative method, and different standard samples depending on the spectral region: coumarin 152 (Φ_{fl} = 0.19 in EtOH) for the blue region [85], PM597 (Φ_{fl} = 0.32 in cHex)[20] for the green and cresyl violet (Φ_{fl} = 0.54 in CH_3OH)[86] and zinc phthalocyanine (Φ_{fl} = 0.30 in 1% pyridine in toluene)[87] for the red-Visible region.

Radiative decay curves were recorded in the same Edinburgh Instrument by *Time-Correlated Single-Photon Counting Technique* (TC-SPC), using a microchannel plate detector (Hamamatsu C4878) with picoseconds time resolution (≈20 ps). Fluorescence decay curves were monitored at the maximum emission wavelength after excitation by means of a fianium supercontinuous wavelength tunable-laser with 150 ps FWHM pulses.

The singlet oxygen ($^1O_2$) production was determined by direct measurement of their phosphorescence at 1276 nm employing NIR detector (InGaAs detector, Hamamatsu G8605-23), integrated into the same Edinburgh spectrofluorimeter upon continuous monochromatic excitation (450 W Xenon lamp) of the sample. Singlet oxygen quantum yields (Φ_Δ^{PS}) were calculated by a relative method, using commercial photosensitizers as references: Rose Bengal (RB, Φ_Δ^{PS} = 0.86 in CH_3OD), MeSBDP (CAS-1835282-63-7, Φ_Δ^{PS} = 0.98 in CH_3OD and Φ_Δ^{PS} = 0.91 in $CHCl_3$)[88] and New Methylene Blue (NMB, Φ_Δ^{PS} = 0.76 in CH_3OD).

The amount of PSs in MSN was estimated photometrically, reading of absorbance value of a previously weighted amount of nanoparticles in a stable suspension and assuming that the molar extinction coefficient of the dye is the same in solution as being grafted at the nanoparticles.

2.6. In vitro Assays

2.6.1. Cell culture

Human cervical adenocarcinoma cells (HeLa cells, CCL2) purchased from ATCC were grown in Dulbecco's modified Eagle's medium (DMEM) supplemented with 10% (v/v) fetal bovine serum (FBS) and 50 U/mL penicillin and 50 mg/mL streptomycin, in a humidified 5% CO_2 cells incubator at 37 ºC. For the cytotoxicity study, cells were grown to monolayer confluency in 96-well microplates. For the internalization and subcellular localization study, cells were seeded in glass-bottom 35 mm Petri dishes and subconfluent monolayers were used.

2.6.2. Sample preparation and *in vitro* exposures

PS-MSNs were suspended in PBS buffer ($1{\cdot}10^{-4}$ M) and stirred for at least 24 h before the exposures. PSs alone were directly dissolved in DMSO ($1{\cdot}10^{-3}$ M). For the *in vitro* exposures, cells were incubated for 24 h with 1, 5, 10, 50 and $100{\cdot}10^{-7}$ M, final concentration of each PS in solution or tethered at MSN nanosystem, in 10% FBS cell culture medium. After 24 h exposure, cells were washed three times with serum-free culture medium and maintained in the culture medium during irradiation (< 30 min, depending on the fluence rate of each light source) and post-treatment time (24 h).

Preprints (www.preprints.org) | NOT PEER-REVIEWED | Posted: 31 May 2021 doi:10.20944/preprints202105.0724.v1

Irradiations were performed using light-emitting diode (LED) devices: LED Par 64 Short Q4-18 (Showtec, Burgebrach, Holland) for blue (λ_{ab} 455 nm) and green (λ_{ab} 518 nm) light and LED 36 W (KINGBO LED) for red (λ_{ab} 655 nm), using a total light dosage (TLD) between 10 and 15 Jcm^{-2}:

$$TLD\ (J/cm^2) = \text{fluence rate}\ (mW/cm^2) \times \text{treatment time}\ (s).$$

The different LEDs were chosen depending on the main absorption band of each sample. Parallel experiments were carried out by incubating the cells with each PS or PS-MSN nanoplatforms without irradiation to test their toxicity in dark conditions. Unexposed cells and cells exposed to 1% DMSO or MSN alone were used as controls. Four replicates of each treatment were used and experiments were repeated three times.

2.6.3. Cell viability (MTT) assay

Dark- and phototoxicity were assessed in HeLa cells using the thiazolyl blue tetrazolium bromide (MTT) assay following the manufacturer's instructions. After exposures, cells were incubated with a 50 µg/mL MTT solution for 3 h at 37 ºC. Then, reduced formazan product was extracted from cells with DMSO and the absorbance was measured at 570 nm in a Biotek EL 312 microplate spectrophotometer reader (Winooski, USA). Cell viability was expressed as the percentage with respect to control cells. Differences between unexposed and treated cells were analyzed through the Kruskal-Wallis test followed by the Dunn's post-hoc test. Differences between dark and light exposures at the same concentrations were analyzed through the Mann-Whitney's U test. EC_{50} values were calculated using the Probit test. All statistical analyses were performed using the SPSS 23.0 software (Chicago, USA). Significance level was globally established at 5% ($p < 0.05$).

3. Results and Discussion

Mesoporous silica nanoparticles with a suitable size for medical applications and particularly for PDT [73,89], were synthesized by the modified Stöber method [90] as described elsewhere [80]. The external surface of mesoporous nanoparticles surface was functionalized with amino group (NH-MSN) or carboxylic group (COOH-MSN). The latter type was obtained after conversion of CN-MSN in acidic conditions, according to the synthesis route described in Figure S3. Bare MSNs analyzed by SEM and TEM showed spherical morphology and mesoporous structure (Figure 2 and Figure S6), with a size distribution of 50±10 nm. The external functionalization of MSNs was studied by XPS (Table S1). The presence of 5% of nitrogen atoms in both NH-MSN and CN-MSN confirmed the existence of amine/cyano functional groups located outside of the nanoparticles whereas the absence of nitrogen atoms in the COOH-MSN indicates an effective conversion of CN into COOH groups. In the case of FTIR spectra (Figure S7), an intense peak located at υ = 1110-1000 cm^{-1} as well as a wide band placed at υ = 3650-3200 cm^{-1} were recorded in every sample spectra, and are assigned to Si-O-C and O-H groups, respectively. A characteristic band of cyane group (C≡N) at υ =2260-2240 $cm^{-1}$was recorded in CN-MSN that disappeared in COOH-MSN system (Figure S7 blue) indicating again the total conversion from -CN to -COOH. Furthermore, the typical band of COOH group (COO-H υ = 3550-2550 cm^{-1}, C=O υ = 1775-1650 cm^{-1}) was also registered in COOH-MSN.

The sizes of the three types of nanosystems were also characterized in water suspension by DLS. Both NH-MSN and COOH-MSN showed similar hydrodynamic diameter, of around 60-70 nm, to the size of the nanoparticles by TEM (Table 1), whereas the larger radio, derived for CN-MSN, of 280 nm, indicates a tendency to form aggregates. Zeta potential values obtained for CN-MSN but also for NH-MSN (≤ ±25 mv) [91] confirm a poorer stability in water with respect to COOH-MSN system. The higher stability of this later functionalized COOH-MSN is attributed to the presence of carboxylic groups at the external surface, partially deprotonated (COO^-) in aqueous media and the superficial negative charge makes the nanosystem more stable by electrostatic repulsion, Table 1.

Preprints (www.preprints.org) | NOT PEER-REVIEWED | Posted: 31 May 2021 doi:10.20944/preprints202105.0724.v1

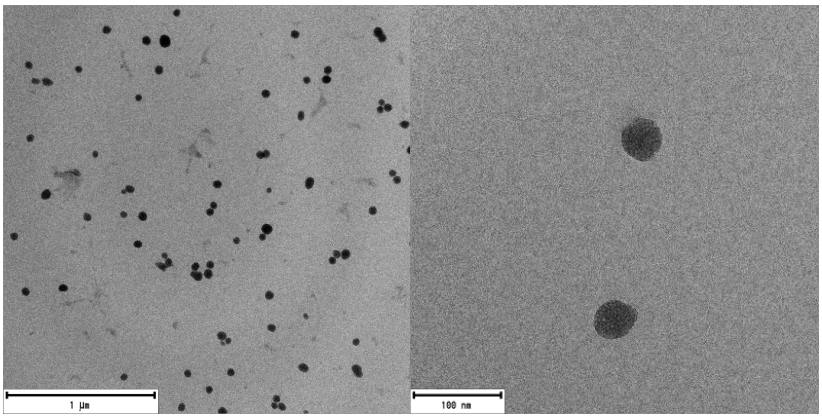

Figure 2. TEM images of MSNs. There are no noticeable differences between all of the synthetized MSNs (NH-MSN, CN-MSN and COOH-MSN)

Table 1. DLS and Zeta potential of mesoporous silica nanoparticles in water.

Name	Shell	DLS (nm)	Z pot (mV)
NH-MSN	NH_2/OH	71	-3.96
CN-MSN	CN/OH	280	-7.06
COOH-MSN	COOH/OH	66	-39.7

Actually, the MSNs stability in aqueous media is certainly controlled by the type and the number of molecules lodged at the external surface. It has been demonstrated that the presence of organic PSs makes the external surface of MNS more hydrophobic promoting nanoparticles agglomeration, hindering their stability in aqueous media [81]. Note here that the particle-particle aggregation is detrimental to singlet oxygen production and should be avoided or minimized. To optimize the PS loading and to ensure the stability of the nanoparticles in suspension, several syntheses were carried out for the amine-functionalized MSN (NH-MSN), employing commercial RB as PS and different PEG derivatives (RB-PEG$_n$-NH-MSN). The combinations were focused on the variation of *i)* the functional group of the MSN (OH-, or NH_2-) at which PS and PEG molecules were attached and *ii)* the length of PEG chain (750 Da, 2000 Da, and 5000 Da).

Rose Bengal is a commercial PS with an intense absorption band (λ_{max} = 556 nm; ε = $9.8 \cdot 10^4$ $M^{-1}cm^{-1}$) and high singlet oxygen production (Φ_Δ=0.86 in CH_3OD). The carboxylic function in the RB molecular structure allows the covalent grafting to be inserted to amine groups or to the intrinsic hydroxyl groups of the external surface of MSN [81]. Nevertheless, both RB-MSN nanosystems (RB grafted at the external NH_2 or OH) showed instantaneous flocculation in water media and the suspension was only viable in less polar solvents. Since stable nanoparticle suspension in water is crucial to obtain competitive hybrid nanocarriers for PDT [81] pegylation of the outside of MSNs is required to avoid the precipitation of the nanoparticles. Firstly, to optimize the stabilization of the system, NHS-PEG of different chain length (750 Da, 2000 Da and 5000 Da) were linked to the amine groups of the silica, while RB was anchored in OH groups (samples RB-PEG$_{750}$-NP-**a**, RB-PEG$_{2000}$-NP-**a**, and RB-PEG$_{5000}$-NP-**a** in Table 2).

Table 2. RB amount, nanoparticle size and their Zeta potential by DLS in water of the different RB-PEG-MSNs

System	Characteristic	PEG length (Da)	DLS size (nm)	Zpot (mV)	[RB] (μmol/g)
RB-PEG$_{750}$-NP-a	RB-OH-MSN PEG-NH_2-MSN	750	130	-4.3	20

Preprints (www.preprints.org) | NOT PEER-REVIEWED | Posted: 31 May 2021 doi:10.20944/preprints202105.0724.v1

RB-PEG$_{2000}$-NP-a	RB-OH-MSN PEG-NH$_2$-MSN	2000	99	-25.0	20
RB-PEG$_{5000}$-NP-a	RB-OH-MSN PEG-NH$_2$-MSN	5000	114	-25.0	20
RB-PEG-NP-b	RB-NH$_2$-MSN PEG-OH-MSN	2000	95	-29.0	10
RB-PEG-NP-c	RB-OH-MSN PEG-OH-MSN	2000	88	-31.0	20

According to zeta potential (Table 2), the lowest value was registered for sample RB-PEG$_{750}$-NP-**a** with the shortest PEG chain in this series, indicating its inefficiency to improve the stability of RB-MSN in water. Indeed, a similar value of around -4 mV was obtained for NH-MSN without RB (Table 1). In contrast, PEG of higher molecular weight, 2000 Da and 5000 Da (RB-PEG$_{2000}$-NP-**a** and RB-PEG$_{5000}$-NP-**a** in Table 2) rendered Zpot values of -25 mV, indicating good stability of these nanosystems in water. The longer PEG-5000 did not lead to an improvement of the stability with respect to PEG-2000, which could likely be assigned to a different conformation adopted at the external surface [92]. Besides, long PEG chains can also impede the internalization of nanoparticles into the cells [93,94]. Thus, PEG of 2000 Da was selected as the most suitable and employed in the rest of the samples.

Next, different anchorages between PEG and MSN (at a fixed PEG length of 2000 Da) were also tested. The anchoring of Si-PEG (silylated PEG of 2000 Da, Figure 1) to the external OH-groups of MSN; samples RB-NP-**b** and RB-NP-**c**, led to even higher Zpot values with respect to sample RB-PEG$_{2000}$-NP-**a** (with PEG at the amine groups), Table 2. This fact is possibly due to a higher presence of PEG at the surface because there are more accessible OH-groups than NH$_2$-groups at the silica external surface [72]. This assumption was confirmed for RB, showing a double dye loading when was tethered to OH with respect to NH$_2$ groups of the MSN external surface (RB-PEG-NP-**b** *vs* RB-PEG-NP-**c** in Table 2) [81].

The stability of the nanoparticles can also be studied by the absorption spectra of the RB-PEG-MSNs samples in water suspension (Figure 2). The registered bands for RB-PEG$_{2000}$-**a** and RB-PEG$_{5000}$-**a**, practically identical, showed more prominent shoulders at both sides of the main absorption band, indicative of a higher dye aggregation tendency. Indeed, according to the absorption spectra, the dye aggregation follows the tendency RB-PEG$_{5000}$-NP-**a** ≈ RB-PEG$_{2000}$-NP-**a** > RB-PEG-NP-**c** > RB-PEG-NP-**b**. For the samples RB-PEG$_{2000}$-NP-**a**, RB-PEG$_{5000}$-NP-**a**, and RB-PEG-NP-**c** (RB grafted at the hydroxyl groups of MSNs, Table 2) the estimated RB loading was equal and consequently, the observed dye aggregation in these samples should be assigned to interparticle processes, as supported by Zpot values and previously attributed to a lower presence of PEG molecules at the external surface. Sample RB-PEG-NP-**b**, with RB loading at the amine groups half of that obtained for the RB at the hydroxyl groups (sample RB-PEG-NP-**b** *vs* sample RB-PEG-NP-**a** in Table 2), showed a narrower absorption band, not much different from that recorded for RB in diluted solution, except for the typical blue-shifted and slight broadening found in dyes in adsorbed-state [80]. However, reducing the cargo of PS per nanoparticle would compel a higher concentration of nanoparticles per volume to reach effective PS doses for PDT in the cells, which would also promote particle-particle agglomeration. For this reason, the optimization of the samples is not a trivial task and the quantification of their singlet oxygen production would be a good indicator for their applicability in cells. Significantly, all the samples, except for RB-PEG$_{750}$-NP-**a**, showed a similar singlet oxygen quantum yield, with values around $\Phi_\Delta \approx 0.80$-0.85 in deuterated methanol (CH_3OD), similar to that registered for RB in the same solvent ($\Phi_\Delta = 0.86$). The fact that RB grafted to MSN can generate singlet oxygen as efficiently as the RB in solution is indicative of the potential use of these nanosystems in PDT [58,60,81].

Preprints (www.preprints.org) | NOT PEER-REVIEWED | Posted: 31 May 2021 doi:10.20944/preprints202105.0724.v1

In this context, we considered MSNs with PS and PEG at OH- groups the best nanosystems for PDT in terms of maximized PS loading with good stability in aqueous media. Nevertheless, in the series of novel in lab-made BODIPY-based PS, homologous molecular structure with carboxyl or silylated groups as graftable groups are proposed (BDP2 *vs* BDP3; BDP4 *vs* BDP5 and BDP6 *vs* BDP7 in Figure 1) to compare their respective PDT action for a normalized concentration of PS incubated in cells. In a further step, FA was anchored through its carboxylic function to the amine groups of NH-MSN to increase the nanosystem internalization into cells, as demonstrated in a former work [80]. The presence of FA at the external surface of PS-PEG-MSNs also assists to the stability of the nanoparticles reducing the interparticle aggregation as it was experimentally verified by the absorption spectra of RB in sample RB-PEG-NP-**d** (Figure 2) in comparison with sample RB-PEG-NP-**c** without FA**,** and whose band shape resembles that of RB in sample of RB-PEG-NP-**b**. The successful tethering of FA at the MSNs was checked by its characteristic band at 350 nm (Figure S8) [80,95], although its accurate quantification was not possible because of the important scatter contribution in this region.

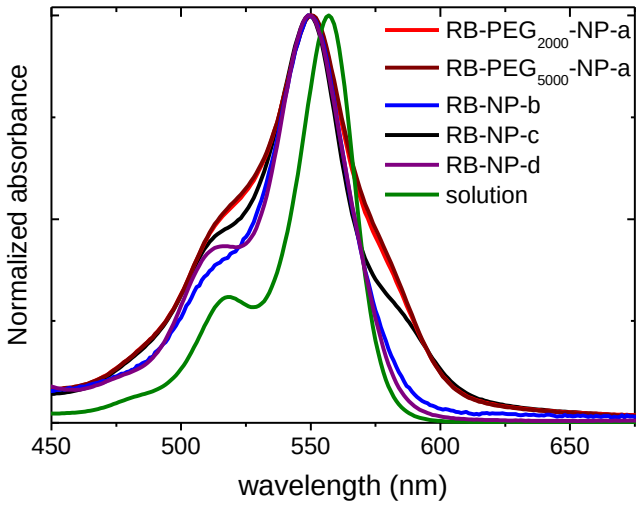

Figure 2. Normalized absorption spectra of RB-PEG$_{2000}$-NP-**a** (red), RB-PEG$_{5000}$-NP-**a** (brown), RB-PEG-NP-**b** (blue), RB-PEG-NP-**c** (black), RB-PEG-NP-**d** (purple) in water suspension (0.5 mg/mL) and RB in diluted CH_3OH solution (green). *The absorption spectra for all samples were recorded after stirring the nanosystems for at least 24 h.*

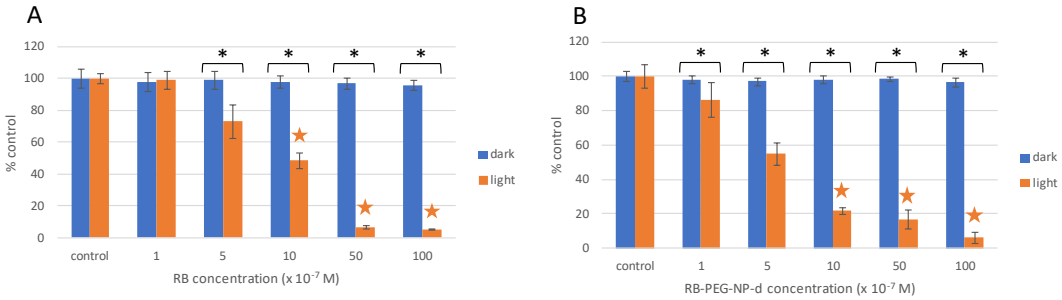

Figure 3. Cell viability (MTT assay) of HeLa cells exposed to different RB concentrations, (A) in solution and (B) tethered at MNS (sample RB-PEG-NP-**d**) under dark conditions (blue bars) and green irradiation at 518 nm and 10 J/cm² (orange bars). Stars indicate significant differences with respect to controls. Asterisks indicate significant differences between dark and light conditions at the same concentrations tested.

Preprints (www.preprints.org) | NOT PEER-REVIEWED | Posted: 31 May 2021 doi:10.20944/preprints202105.0724.v1

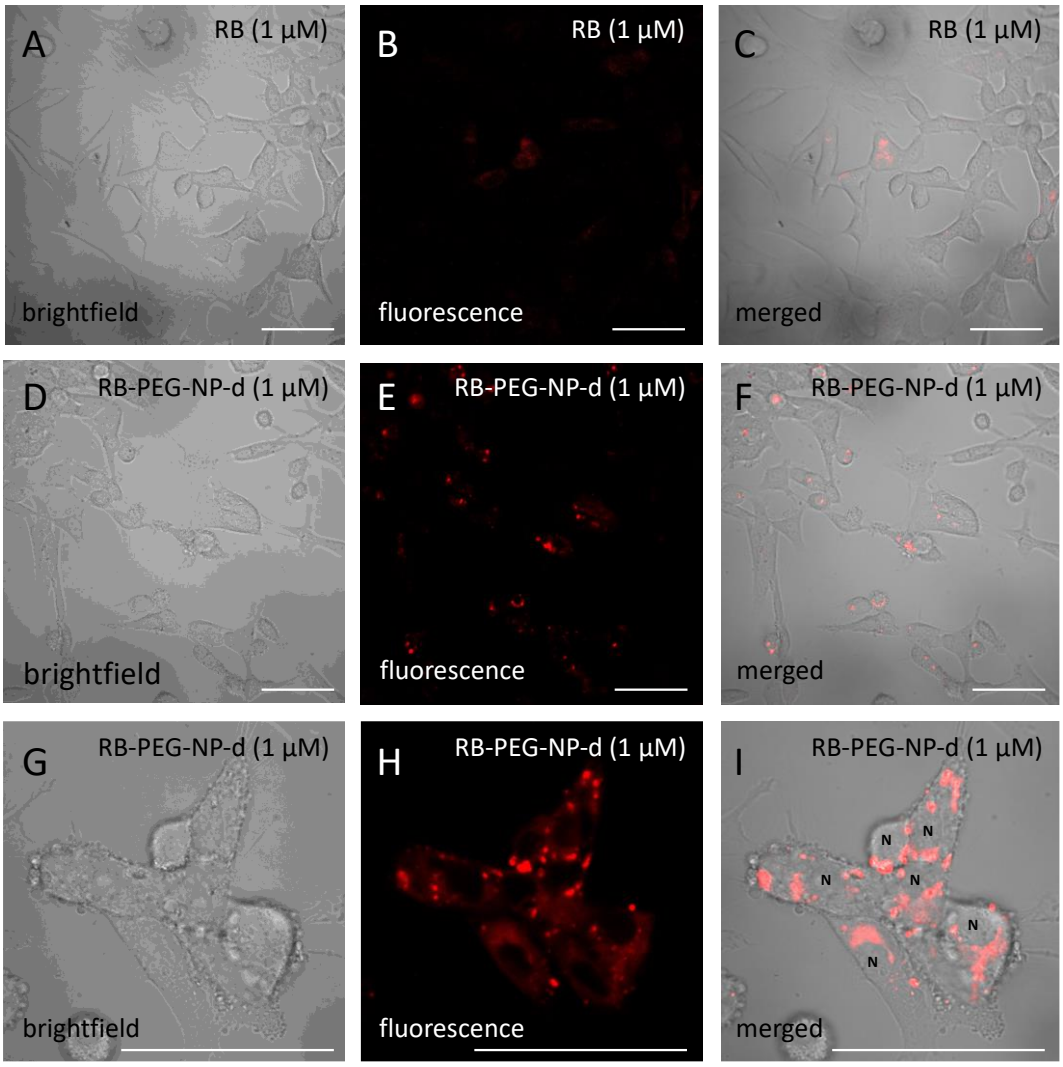

Figure 4 Confocal fluorescence microscopy images of HeLa cells exposed to RB free in solution (A-C) and cells exposed to RB-PEG-NP-**d** (D-I) at the same RB concentration (1 µM). Scale bars = 100 µm.

Based on the *in vitro* experiments, both RB-PEG-NP-**d** (RB and PEG grafted at the OH- and FA at NH_2-) and RB free in solution were not cytotoxic under dark conditions (Figure 3, Tables S3 and S4). When exposed to light, RB-PEG-NP-**d** showed a higher phototoxicity compared to RB in solution at the same PS concentration (Figure 3 and Tables S3 and S4). At a normalized RB concentration of 1 µM, RB-PEG-NP-**d** decreased 80% of cell viability, while RB alone in solution decreased 50% of cell viability (Figure 3). EC_{50} value for RB-PEG-NP-**d** exposure was 0.55 µM while in exposure to RB alone was 1.05 µM (Tables S3 and S4). This is probably related to a higher internalization of the RB-PEG-NP-**d** compared to RB in solution as can be seen in Figure 4. Indeed, previous internalization assays of analog PEG-FA-MSNs but functionalized with a fluorescent dye (Rhodamine 101) demonstrated the capability of these nanosystems to accumulate specifically inside lysosomes of HeLa cells [80].

Concerning the in-lab synthesized PSs, the molecular design of the novel lab-made BODIPY-PSs was based on previous studies [18,28,96–98]. The best choice to promote the intersystem crossing in haloBODIPY is the iodination at the 2 and 6 positions of the BODIPY core (BDP2 and BDP3), reaching singlet oxygen production ≥ 80% under green illumination (Table S1). Another alternative without using halide atoms to preclude the cytotoxic effect inherent to heavy atoms [21,31,99–101], is based on orthogonal BODIPY

Preprints (www.preprints.org) | NOT PEER-REVIEWED | Posted: 31 May 2021 doi:10.20944/preprints202105.0724.v1

dimers [102] (BDP4 and BDP5). Generally, these dyads are endowed with very intense absorption bands in the green region as well as high singlet oxygen generation ($\Phi_\Delta > 75\%$, Table S1) promoted by intra charge transfer states [103–105]. To shift the absorption band to the blue region (BDP1), a nitrogen atom was placed at *meso* position of the BODIPY together with iodines at 2 and 6. The formation of hemicyanine-like structure induced a very pronounced blue-shift, placing the main absorption band in the blue region (at around 420-440 nm) [27] but keeping a good singlet oxygen generation (≈ 80%, Table S1). Most interestingly for PDT, to shift the absorption into the clinic window (650-850 nm), conjugated systems [98], particularly styryl groups with electron-donating methoxy groups in 3 and 4 positions of phenyl ring, were added at 3 and 5 positions, accompanied by iodine atoms at 2 and 6 positions (BDP6 and BDP7). The singlet oxygen quantum yield achieved for these red-haloBODIPYs, was lower, of around 45% (Table S1) with respect the other BDP-PS in this series, but they revealed emission ability around 20% which can enable fluorescence imaging, in contrast with the rest of non-emissive haloBDP ($\Phi_{fl} \leq 0.03$, Table S2). Additionally, graftable groups were also incorporated in *meso* position to all these BODIPYs to allow their linking to MSNs.

Thus, PSs (commercial and lab-made) were classified according to their absorption range (blue, green and red) and their respective graftable groups (silylated: BDP1, BDP3, BDP5 and BDP7; carboxylic: C6, BDP2, BDP4 and BDP6; and amine group: Th, Figure 1). The outer surface of MSNs was also decorated with PEG and FA, tethering at the hydroxyl groups of MSN and at amine groups, respectively except for the COOH-MSN in which a modified folic acid, FA-HDA (see Figure S4) was linked to the carboxylic groups.

The photophysical features, the singlet oxygen production and the phototoxic action of PS-PEG-FA-MSNs in HeLa cells were compared with their chemically homologous PSs with carboxylic group since the silylated ones polymerize in cell culture media (Table 3, Table S2 and Figure 3).

The absorption spectra of PS-MSNs together with the respective PSs in solution are shown in Figure 5. Generally, the absorption bands appeared broader and slightly blue-shifted with respect to the PS in solution (Figure 5 brown), characteristic effect found for dyes anchored at a surface, although the formation of molecular aggregates cannot be totally discarded in the same cases [80], Figure 2. Importantly, the singlet oxygen yields in most of PS-PEG-FA-MSN systems in suspension were in good agreement with the PS in solution (Table 3 *vs* Table S1), particularly for the samples BDP4-NP, BDP5-NP, BDP6-NP, C6-NP and Th-NP. Note that the high amount of PS finally loaded in the MSNs for samples BDP1-NP and BDP3-NP could be the reason for the observation of a slightly lower value of the singlet oxygen production, likely associated to intra-particle dye-dye aggregation. On the opposite, PS loading in samples BDP2-NP and BDP7-NP was insufficient (3 μmol/g, Table 3) to get accurate values of singlet oxygen quantum yields, and for the same reason, these later samples were not considered suitable to be applied for PDT.

Table 3. Cargo of PS at MSNs, absorption maxima (λ_{ab}) and the singlet oxygen quantum yield in CH_3OD (Φ_Δ) measured after stirring the suspensions for 24 h of the PS-PEG-FA-MSN systems

System	Characteristic	[PS] (μmol/g)	λ_{ab} (nm)	Φ_Δ
BDP1-NP	BDP1-OH-MSN PEG-OH-MSN FA-NH_2-MNS	30	435.0	0.62
BDP2-NP	BDP2-NH_2-MSN PEG-OH-MSN FA-NH_2-MNS	3	527.0	-
BDP3-NP	BDP3-OH-MSN	40	528.0	0.69

Preprints (www.preprints.org) | NOT PEER-REVIEWED | Posted: 31 May 2021 doi:10.20944/preprints202105.0724.v1

	PEG-OH-MSN FA-NH_2-MNS BDP4-NH_2-MSN			
BDP4-NP	PEG-OH-MSN FA-NH_2-MNS	5	513.0	0.81
	BDP5-OH-MSN			
BDP5-NP	PEG-OH-MSN FA-NH_2-MNS	11	511.0	0.73
	BDP6-NH_2-MSN			
BDP6-NP	PEG-OH-MSN FA-NH_2-MNS	7	670.0	0.50
	BDP7-OH-MSN			
BDP7-NP	PEG-OH-MSN FA-NH_2-MNS	3	669.5	-
	C6-NH_2-MSN			
C6-NP	PEG-OH-MSN FA-NH_2-MNS	6	662.0	0.82
	Th-COOH-MSN			
Th-NP	PEG-OH-MSN FA-HDA-COOH-MNS	15	599.0	0.84

The most representative lab-made PS-MSNs were tested in HeLa cells applying different light sources depending on the absorption band positions: BDP1-NP (λ_{max} = 435 nm) under blue irradiation (λ_{max} = 435 nm at 10 J/cm^2), BDP3-NP, BDP4-NP and BDP5-NP (λ_{max} = 510-530 nm) under green irradiation (λ_{max} = 518 nm at 10 J/cm^2) and finally C6-NP and BDP6-NP (λ_{max} =635-660 nm) were irradiated under red light (λ_{max} = 655 nm at 15 J/cm^2). Unfortunately none of our available irradiation sources (blue, green or red, see experimental section) were suitable to activate the Th photosensitizer (λ_{ab} ≈ 600nm).

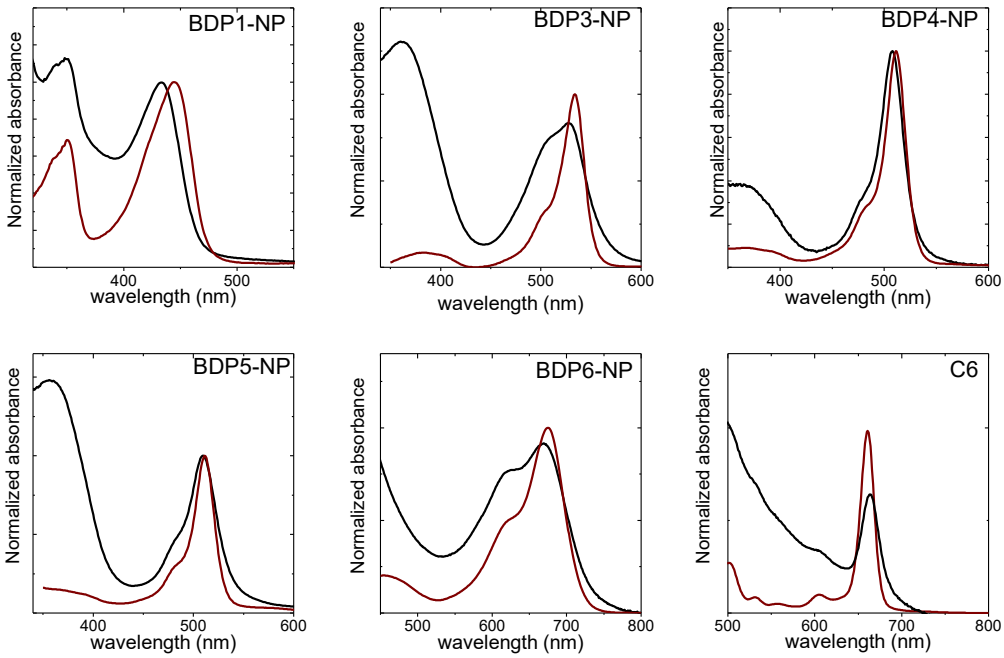

Figure 5. Normalized absorption spectra of PS in $CHCl_3$ solution (brown) and the PS tethered at the

 doi:10.20944/preprints202105.0724.v1

external surface of MSN together with PEG and FA (black) in CH_3OH at 0.5 mg/mL. *The absorption spectra for all the PS-MSN samples were recorded after stirring the nanosystems for at least 24 h.*

At dark conditions, some PSs free in solution such as halo-BODIPY, BDP2 and BDP6, as well as the commercial C6 were toxic to HeLa cells at concentrations ≥1 μM (Figures 6, 7, Table S3). On the other hand, when these PSs were grafted to the MSNs no cytotoxicity was observed at dark conditions (Figure 6, Figure 7 and Figure S9). In general terms, PS-PEG-FA-MSN did not show any toxicity under dark conditions (Table S4), except for BDP4-NP (Figure S10), sample with a low PS loading at the MSN (5 μmol/g, Table 3) which required a higher amount of nanoparticles (≈0.9 mg/mL) to achieve an equal PS concentration of 5 μM incubated in HeLa cells. To avoid cytotoxicity and to guarantee the safe use of PS-PEG-FA-MSN, the upper limit was set at 1 mg/mL, value in good agreement with a former work [80].

BDP1-NP nanosystem was able to induce around 70% of cell death at 1 μM of PS concentration and near 90% cell death at 5 μm under blue light irradiation, leading to a EC_{50} = 1.0 μM (Figure S9). Better performance was revealed by the haloBDP nanosystem BDP3-NP activated by green irradiation light, which induced ≥ 80% cytotoxicity under light exposure at 0.5 μM PS and ≥ 90% at 1 μM PS (Figure 6A) providing an EC_{50} of 0.4 μM (Table S4) without any cytotoxic effects in dark conditions. However, although the homologous haloBDP BDP2 free in solution induced higher phototoxicity under light conditions (Figure 6B, Table S3), attributed to a higher oxygen singlet production than PS at the MSN surface (Φ_Δ = 0.95 *vs* 0.70, Tables 3 and S1, respectively) it also induced cytotoxicity in dark conditions (EC_{50}(DARK) ≈ 4 mM, Table S3). Conversely, halogen-free BODIPY dimer BDP4 did not show toxicity in dark but its phototoxicity action was also very reduced (Figure 6C). However, the fact that this heavy-atom free PS did not show dark toxicity allows a safe increase of the dimer incubated doses, reaching a 75% and 90% decrease of cell viability at 5 μM and 10 μM PS concentrations, respectively (Figure 6C).

Note that the phototoxicity is drastically enhanced when the BODIPY dimer is loaded at the MSN surface (*e.g.* BDP5-NP) leading to an EC_{50} value 40 times higher (Tables S3 and S4). The Figures 6C-D show how BDP5-NP induced a decrease of 90-100% in HeLa viability at 0.5 μM, whereas nearly no phototoxicity was observed for the BODIPY dimer at the same concentration. The lower cytotoxicity effect under light irradiation of BDP4, a larger molecule with a lesser solubility in aqueous solution, could be likely assigned to a poor internalization into the cells.

These promising results demonstrated the efficiency of functionalized MSNs to successfully transport PSs into HeLa cells promoting higher phototoxicity at a lower concentration of PSs in comparison with the PS free in solution and avoiding cytotoxicity under dark conditions. Most importantly, the proposed BDP-PEG-FA-MSNs (both iodinated and orthogonal BODIPY dimers) showed a higher phototoxicity effect in comparison with analogous nanosystems loaded with commercial RB under the same green light doses (Figures 3 and 6, and Table S4).

Preprints (www.preprints.org) | NOT PEER-REVIEWED | Posted: 31 May 2021 doi:10.20944/preprints202105.0724.v1

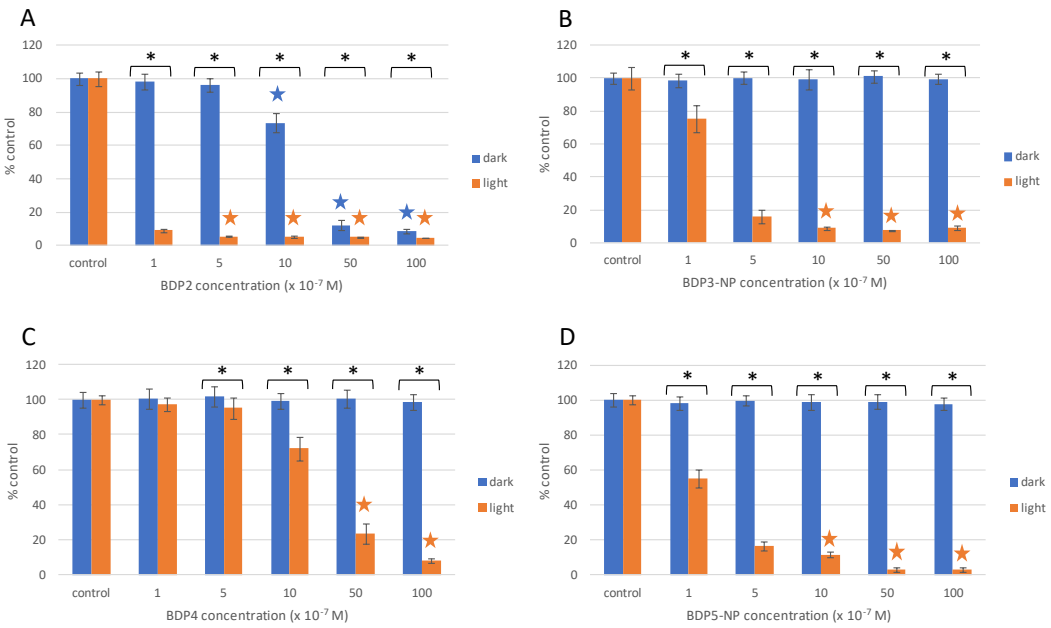

Figure 6. Cell viability (MTT assay) of HeLa cells exposed to the PSs in solution BDP2 (A) and BDP4 (C) and to their corresponding nanosystems BDP3-NP (B) and BDP5-NP (D) under dark conditions (blue bars) and after green irradiation at 10 J/cm^2 (orange bars). Stars indicate significant differences with respect to controls. Asterisks indicate significant differences between dark and light conditions at the same concentrations tested.

The designed BDP-based PSs for red-irradiation generally displayed lower phototoxicity with respect to those in the green region (Figure 7 *vs* Figure 6), which is in agreement with their lower oxygen singlet production (Table 3 and Table S2). However, the red-BODPY-PS have demonstrated a higher ability to kill cells under red light irradiation than the commercial and widely used C6 despite a lower oxygen singlet production with respect to C6. The lower oxygen singlet production is balanced with a higher absorption coefficient, reaching higher phototoxicity (Table S2) resulting in lower EC_{50} under red light irradiation (Table S3) but also higher cytotoxicity in dark condition (Figures 7A-C).

Although the photoactivity of the red-PSs loaded at MSN, samples BDP6-NP and C6-NP, respect to PSs free in solution was inferior; once again, MSNs hampered the inherent toxicity of PSs in dark, which is of interest for clinical studies. In this context, PDT efficiency could be increased by safely applying higher concentrations of PS-MSNs and by increasing the exposure time of the irradiation [106]. Besides, these functionalized nanosystems loaded with red-BDP PS are endowed with enough brightness to be tracked by fluorescence microscopy (Figure S11).

Preprints (www.preprints.org) | NOT PEER-REVIEWED | Posted: 31 May 2021 doi:10.20944/preprints202105.0724.v1

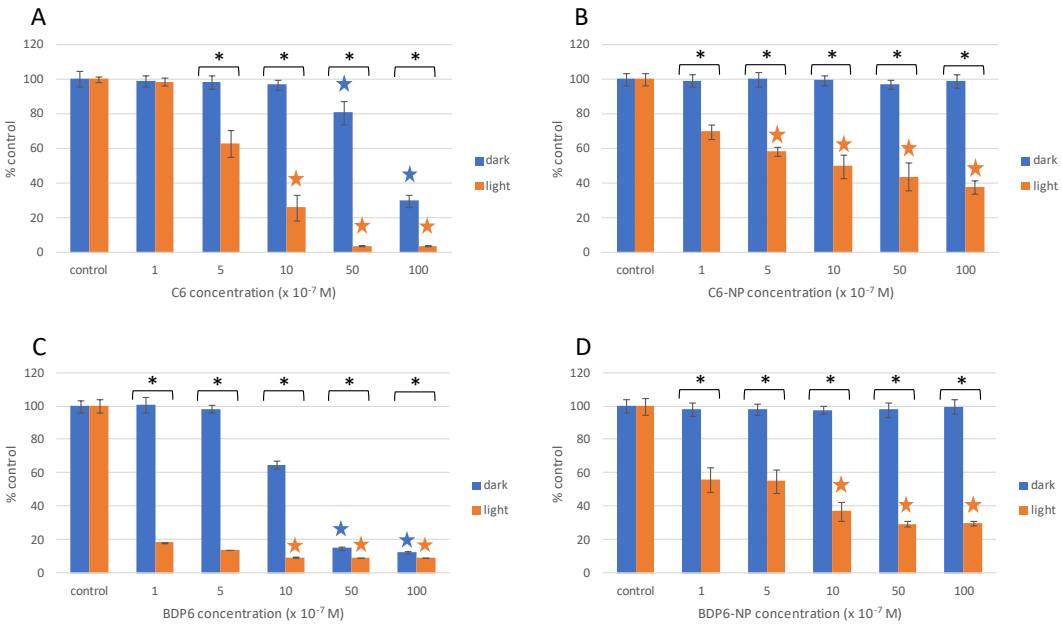

Figure 7. Cell viability (MTT assay) of HeLa cells exposed to PSs in solution C6 (A) and BDP6 (C) and to their respective the nanosystems C6-NP (B), and BDP6-NP (D) under dark conditions (blue bars) and after red irradiation at 15 J/cm^2 (orange bars). Stars indicate significant differences with respect to controls. Asterisks indicate significant differences between dark and light conditions at the same concentrations tested.

4. Conclusion

Photosensitized silica nanoparticles functionalized with PEG and FA proved to be suitable and biocompatible nanosystems able to overcome some of the PS drawbacks: i) avoid cytotoxicity under dark conditions ensuring safe use in clinical trials for cancer treatment; ii) increase their internalization providing a better PDT performance in HeLa cells in comparison with PSs free in solution. Overall, photosensitized silica nanoparticles with BODIPY-based PSs have shown higher phototoxicity compared to commercial PSs (*i.e.* RB-NP *vs* BDP3-NP or BDP5-NP under green light and C6-NP *vs* BDP6-NP under red light irradiation). Finally, BDP-PEG-FA-MSN systems under red light irradiation have also enabled fluorescence bioimaging, making them promising platforms to be implemented in PDT.

Supplementary Materials: The following are available online at www.mdpi.com/xxx/s1, Scheme S1: Synthesis of BODIPYs BDP1-BDP7. Reaction conditions: i) NH_2-$(CH_2)_3$-Si$(OEt)_3$, CH_3CN/CH_2Cl_2 (1:1), rt; ii) APTES, TEA, EDC, HOBt, CH_2Cl_2, rt; iii) 2,4-dimethylpyrrole, TFA, DDQ, TEA, BF_3. Et_2O, CH_2Cl_2, rt; iv) 3,4-dimethoxybenzaldehyde, piperidine, AcOH, DMF, 80 ºC, MW, Figure S1: Synthesis of NH-MSN,Figure S2: Synthesis of CN-MSN, Figure S3: Synthesis of COOH-MSN from CN-MSN, Scheme S2: Folic acid (FA) structure and their derivate FA-HDA-Boc and FA-HDA, Figure S4: Synthesis of folic acid derivate FA-HDA-Boc, Figure S5: Deprotection of FA-HDA-Boc to obtain FA-HDA, Figure S6: SEM image of MSNs, Table S1: XPS data of mesoporous silica nanoparticles in water, Figure S7: Infrared spectra of NH-MSN (black), CN-MSN (red) and COOH-MSN (blue) and from 2500 cm^{-1} to 2150 cm^{-1} (inset), Figure S8: Normalized absorption spectra of folic acid (blue) and RB-PEG-NP-d (purple) in aqueous solution (0.5 mg/mL), Table S2: Photophysical parameters and singlet oxygen quantum yields for graftable-PSs; absorption maxima (λ_{ab}), molar absorption coefficient (ε_{max}), fluorescence maxima (λ_{fl}), fluorescence quantum yield (Φ_{fl}), fluorescence lifetime (τ_{fl}), singlet oxygen quantum yield (Φ_{Δ}) and Phototoxic Power (PP = $\varepsilon \cdot \Phi_{\Delta}$), Figure S9: Cell viability (MTT assay) of HeLa cells exposed to for the nanosystem BDP1-NP, in dark conditions (blue) and after blue irradiation at 10 J/cm^2 (red). Stars indicate significant differences with respect to controls. Asterisks indicate significant differences between dark and light conditions at the same concentration, Figure S10: Cell viability (MTT assay) of HeLa cells exposed to the nanosystem BDP4-NP, in dark conditions (blue) and after green irradiation at 10 J/cm^2 (red). Stars indicate significant differences with respect to controls. Asterisks indicate significant differences

between dark and light conditions at the same concentration, Table S3: EC_{50} in HeLa cells treated with PSs with carboxylic group for 24 h given as PS concentration, Table S4: EC_{50} in HeLa cells treated with PS-NPs for 24 h given as PS concentration, Figure S11: Fluorescence microscopy images of HeLa cells treated with 1 μM BDP6-NP for 24 h. Scale bars = 100 μm and ^{1}H NMR and ^{13}C NMR spectra.

Author Contributions: Conceptualization, V.M.-M.; methodology, R.P-M., A.P.C., A.K. and V.M.-M.; writing—original draft preparation, R.P-M., A.K. and V.M.-M.; writing—review and editing, R.P-M., A.K., M.P.C., A.R.A., M.J.O. and V.M.-M.; supervision, V.M.-M, M.P.C., and M.J.O.; funding acquisition, M.P.C., M.J.O. and V.M.-M. All authors have read and agreed to the published version of the manuscript.

Funding: This research was funded by the Basque Government, grant numbers IT912-16 and IT-1302-19, Ministry of Economy and Competitiveness (MINECO), grant numbers MAT2017-83856-C3-2-P, MAT2017-83856-C3-3-P, PID2020-114755GB-C3 and CTM2016-81130-R; and the University of the Basque Country (UPV/EHU), grant number COLAB19/01.

Data Availability Statement: In this section, please provide details regarding where data supporting reported results can be found, including links to publicly archived datasets analyzed or generated during the study. Please refer to suggested Data Availability Statements in section "MDPI Research Data Policies" at https://www.mdpi.com/ethics. You might choose to exclude this statement if the study did not report any data.

Acknowledgments: We would like to thank the Advanced Research Facilities (SGIker) of the University of the Basque Country for the support on confocal microscopy image analysis.

Conflicts of Interest: The authors declare no conflict of interest. The funders had no role in the design of the study; in the collection, analyses, or interpretation of data; in the writing of the manuscript, or in the decision to publish the results.

References

1. Dolmans, D.E.J.G.J.; Fukumura, D.; Jain, R.K. Photodynamic therapy for cancer. *Nature Reviews Cancer* **2003**, *3*, 380–387.
2. Dąbrowski, J.M.; Arnaut, L.G. Photodynamic therapy (PDT) of cancer: From local to systemic treatment. *Photochemical and Photobiological Sciences* **2015**, *14*, 1765–1780.
3. Hopper, C. Photodynamic therapy: A clinical reality in the treatment of cancer. *Lancet Oncology* **2000**, *1*, 212–219.
4. Moghissi, K.; Dixon, K.; Gibbins, S. A Surgical View of Photodynamic Therapy in Oncology: A Review. *The Surgery Journal* **2015**, *01*, e1–e15.
5. Lin, J.; Wan, M.T. Current evidence and applications of photodynamic therapy in dermatology. *Clinical, Cosmetic and Investigational Dermatology* **2014**, *7*, 145–163.
6. DeRosa, M. Photosensitized singlet oxygen and its applications. *Coordination Chemistry Reviews* **2002**, *233–234*, 351–371.
7. Nonell, S.; Flors, C. *Singlet Oxygen, Applications in Biosciences and Nanosciences*; Nonell, S., Flors, C., Eds.; Royal Society of Chemistry: Cambridge, 2016; ISBN 978-1-78262-038-9.
8. Huang, Z. *A review of progress in clinical photodynamic therapy*; 2005; Vol. 4;.
9. Stallivieri, A.; Colombeau, L.; Jetpisbayeva, G.; Moussaron, A.; Myrzakhmetov, B.; Arnoux, P.; Acherar, S.; Vanderesse, R.; Frochot, C. Folic acid conjugates with photosensitizers for cancer targeting in photodynamic therapy: Synthesis and photophysical properties. *Bioorganic & Medicinal Chemistry* **2017**, *25*, 1–10.
10. Lacombe, S.; Pigot, T. Materials for selective photo-oxygenation vs. photocatalysis: Preparation, properties and applications in environmental and health fields. *Catalysis Science and Technology* **2016**, *6*, 1571–1592.
11. Lucky, S.S.; Soo, K.C.; Zhang, Y. Nanoparticles in Photodynamic Therapy. *Chemical Reviews* **2015**, *115*, 1990–2042.
12. Yin, R.; Hamblin, M. Antimicrobial Photosensitizers: Drug Discovery Under the Spotlight. *Current Medicinal Chemistry* **2015**, *22*, 2159–2185.
13. Li, X.; Kolemen, S.; Yoon, J.; Akkaya, E.U. Activatable Photosensitizers: Agents for Selective Photodynamic Therapy. *Advanced Functional Materials* **2017**, *27*, 1–11.

14. Blázquez-Moraleja, A.; Álvarez-Fernández, D.; Prieto-Montero, R.; García-Moreno, I.; Martínez-Martínez, V.; Bañuelos, J.; Sáenz-de-Santa-María, I.; Chiara, M.D.; Chiara, J.L. A general modular approach for the solubility tagging of BODIPY dyes. *Dyes and Pigments* **2019**, *170*, 107545–107556.
15. Zhang, X.F.; Yang, X. Photosensitizer that selectively generates singlet oxygen in nonpolar environments: Photophysical mechanism and efficiency for a covalent BODIPY dimer. *Journal of Physical Chemistry B* **2013**, *117*, 9050–9055.
16. Guan, Q.; Zhou, L.; Li, Y.; Dong, Y. Diiodo-Bodipy-Encapsulated Nanoscale Metal–Organic Framework for pH-Driven Selective and Mitochondria Targeted Photodynamic Therapy. *Inorganic Chemistry* **2018**, *57*, 10137–10145.
17. Sánchez-Arroyo, A.J.; Palao, E.; Agarrabeitia, A.R.; Ortiz, M.J.; García-Fresnadillo, D. Towards improved halogenated BODIPY photosensitizers: clues on structural designs and heavy atom substitution patterns. *Physical Chemistry Chemical Physics* **2017**, *19*, 69–72.
18. Prieto-Montero, R.; Prieto-Castañeda, A.; Sola-Llano, R.; Agarrabeitia, A.R.; García-Fresnadillo, D.; López-Arbeloa, I.; Villanueva, A.; Ortiz, M.J.; Moya, S.; Martínez-Martínez, V. Exploring BODIPY Derivatives as Singlet Oxygen Photosensitizers for PDT. *Photochemistry and Photobiology* **2020**, *96*, 458–477.
19. López Arbeloa, F.; Bañuelos, J.; Martínez, V.; Arbeloa, T.; López Arbeloa, I. Structural, photophysical and lasing properties of pyrromethene dyes. *International Reviews in Physical Chemistry* **2005**, *24*, 339–374.
20. Prieto, J.B.; Arbeloa, F.L.; Martínez, V.M.; López, T.A.; Arbeloa, I.L. Photophysical properties of the pyrromethene 597 dye: Solvent effect. *Journal of Physical Chemistry A* **2004**, *108*, 5503–5508.
21. Turksoy, A.; Yildiz, D.; Akkaya, E.U. Photosensitization and controlled photosensitization with BODIPY dyes. *Coordination Chemistry Reviews* **2019**, *379*, 47–64.
22. Zhang, X.F.; Feng, N. Photoinduced Electron Transfer-based Halogen-free Photosensitizers: Covalent meso-Aryl (Phenyl, Naphthyl, Anthryl, and Pyrenyl) as Electron Donors to Effectively Induce the Formation of the Excited Triplet State and Singlet Oxygen for BODIPY Compounds. *Chemistry - An Asian Journal* **2017**, *12*, 2447–2456.
23. Jiménez, J.; Prieto-Montero, R.; Maroto, B.L.; Moreno, F.; Ortiz, M.J.; Oliden-Sánchez, A.; López-Arbeloa, I.; Martínez-Martínez, V.; de la Moya, S. Manipulating Charge-Transfer States in BODIPYs: A Model Strategy to Rapidly Develop Photodynamic Theragnostic Agents. *Chemistry - A European Journal* **2020**, *26*, 601–605.
24. Kim, B.; Sui, B.; Yue, X.; Tang, S.; Tichy, M.G.; Belfield, K.D. In Vitro Photodynamic Studies of a BODIPY-Based Photosensitizer. *European Journal of Organic Chemistry* **2017**, *2017*, 25–28.
25. Ziessel, R.; Ulrich, G.; Haefele, A.; Harriman, A. An artificial light-harvesting array constructed from multiple bodipy dyes. *Journal of the American Chemical Society* **2013**, *135*, 11330–11344.
26. Wang, D.G.; Zhang, L.N.; Li, Q.; Yang, Y.; Wu, Y.; Fan, X.; Song, M.; Kuang, G.C. Dimeric BODIPYs with different linkages: A systematic investigation on structure-properties relationship. *Tetrahedron* **2017**, *73*, 6894–6900.
27. Esnal, I.; Valois-Escamilla, I.; Gõmez-Durán, C.F.A.; Urías-Benavides, A.; Betancourt-Mendiola, M.L.; Lõpez-Arbeloa, I.; Bañuelos, J.; García-Moreno, I.; Costela, A.; Peña-Cabrera, E. Blue-to-orange color-tunable laser emission from tailored boron-dipyrromethene dyes. *ChemPhysChem* **2013**, *14*, 4134–4142.
28. Epelde-Elezcano, N.; Martínez-Martínez, V.; Peña-Cabrera, E.; Gómez-Durán, C.F.A.; Arbeloa, I.L.; Lacombe, S. Modulation of singlet oxygen generation in halogenated BODIPY dyes by substitution at their *meso* position: towards a solvent-independent standard in the vis region. *RSC Adv.* **2016**, *6*, 41991–41998.
29. Loudet, A.; Burgess, K. BODIPY dyes and their derivatives: Syntheses and spectroscopic properties. *Chemical Reviews* **2007**, *107*, 4891–4932.
30. Bañuelos, J. BODIPY Dye, the Most Versatile Fluorophore Ever? *Chemical Record* **2016**, *16*, 335–348.
31. Kamkaew, A.; Lim, S.H.; Lee, H.B.; Kiew, L.V.; Chung, L.Y.; Burgess, K. BODIPY dyes in photodynamic therapy. *Chemical Society reviews* **2013**, *42*, 77–88.
32. Palao-Utiel, E.; Montalvillo-Jiménez, L.; Esnal, I.; Prieto-Montero, R.; Agarrabeitia, A.R.; García-Moreno, I.; Bañuelos, J.; López-Arbeloa, I.; de la Moya, S.; Ortiz, M.J. Controlling Vilsmeier-Haack processes in meso-methylBODIPYs: A new way

to modulate finely photophysical properties in boron dipyrromethenes. *Dyes and Pigments* **2017**, *141*, 286–298.

33. Chaturvedi, V.K.; Singh, A.; Singh, V.K.; Singh, M.P. Cancer Nanotechnology: A New Revolution for Cancer Diagnosis and Therapy. *Current Drug Metabolism* **2018**, *20*, 416–429.
34. Dawidczyk, C.M.; Kim, C.; Park, J.H.; Russell, L.M.; Lee, K.H.; Pomper, M.G.; Searson, P.C. State-of-the-art in design rules for drug delivery platforms: Lessons learned from FDA-approved nanomedicines. *Journal of Controlled Release* **2014**, *187*, 133–144.
35. Mirabello, V.; Calatayud, D.G.; Arrowsmith, R.L.; Ge, H.; Pascu, S.I. Metallic nanoparticles as synthetic building blocks for cancer diagnostics: from materials design to molecular imaging applications. *J. Mater. Chem. B* **2015**, *3*, 5657–5672.
36. Bobo, D.; Robinson, K.J.; Islam, J.; Thurecht, K.J.; Corrie, S.R. Nanoparticle-Based Medicines: A Review of FDA-Approved Materials and Clinical Trials to Date. *Pharmaceutical Research* **2016**, *33*, 2373–2387.
37. Zhuang, Y.; Zhao, L.; Zheng, L.; Hu, Y.; Ding, L.; Li, X.; Liu, C.; Zhao, J.; Shi, X.; Guo, R. LAPONITE-Polyethylenimine Based Theranostic Nanoplatform for Tumor-Targeting CT Imaging and Chemotherapy. *ACS Biomaterials Science and Engineering* **2017**, *3*, 431–442.
38. Alexis, F.; Pridgen, E.; Molnar, L.K.; Farokhzad, O.C. Factors affecting the clearance and biodistribution of polymeric nanoparticles. *Molecular Pharmaceutics* **2008**, *5*, 505–515.
39. Mousa, M.; Evans, N.D.; Oreffo, R.O.C.; Dawson, J.I. Clay nanoparticles for regenerative medicine and biomaterial design: A review of clay bioactivity. *Biomaterials* **2018**, *159*, 204–214.
40. Rudramurthy, G.R.; Swamy, M.K. Potential applications of engineered nanoparticles in medicine and biology: an update. *JBIC Journal of Biological Inorganic Chemistry* **2018**, *23*, 1185–1204.
41. Conde, J.; Dias, J.T.; GrazÃº, V.; Moros, M.; Baptista, P. V.; de la Fuente, J.M. Revisiting 30 years of biofunctionalization and surface chemistry of inorganic nanoparticles for nanomedicine. *Frontiers in Chemistry* **2014**, *2*, 1–27.
42. Adumeau, L.; Genevois, C.; Roudier, L.; Schatz, C.; Couillaud, F.; Mornet, S. Impact of surface grafting density of PEG macromolecules on dually fluorescent silica nanoparticles used for the in vivo imaging of subcutaneous tumors. *Biochimica et Biophysica Acta (BBA) - General Subjects* **2017**, *1861*, 1587–1596.
43. Son, J.; Yang, S.M.; Yi, G.; Roh, Y.J.; Park, H.; Park, J.M.; Choi, M.; Koo, H. Folate-modified PLGA nanoparticles for tumor-targeted delivery of pheophorbide a in vivo. *Biochemical and Biophysical Research Communications* **2018**, *498*, 523–528.
44. Zhang, Q.; Liu, F.; Nguyen, K.T.; Ma, X.; Wang, X.; Xing, B.; Zhao, Y. Multifunctional Mesoporous Silica Nanoparticles for Cancer-Targeted and Controlled Drug Delivery. *Advanced Functional Materials* **2012**, *22*, 5144–5156.
45. Villaverde, G.; Baeza, A.; Melen, G.J.; Alfranca, A.; Ramirez, M.; Vallet-Regí, M. A new targeting agent for the selective drug delivery of nanocarriers for treating neuroblastoma. *J. Mater. Chem. B* **2015**, *3*, 4831–4842.
46. Ribeiro, T.; Prazeres, T.J. V; Moffitt, M.; Farinha, J.P.S. Enhanced Photoluminescence from Micellar Assemblies of Cadmium Sulfide Quantum Dots and Gold Nanoparticles. *The Journal of Physical Chemistry C* **2013**, *117*, 3122–3133.
47. Pérez, N.; Ruiz-Rubio, L.; Vilas, J.L.; Rodríguez, M.; Martinez-Martinez, V.; León, L.M. Synthesis and characterization of near-infrared fluorescent and magnetic iron zero-valent nanoparticles. *Journal of Photochemistry and Photobiology A: Chemistry* **2016**, *315*, 1–7.
48. Jeevanandam, J.; Barhoum, A.; Chan, Y.S.; Dufresne, A.; Danquah, M.K. Review on nanoparticles and nanostructured materials: history, sources, toxicity and regulations. *Beilstein Journal of Nanotechnology* **2018**, *9*, 1050–1074.
49. Malvindi, M.A.; Brunetti, V.; Vecchio, G.; Galeone, A.; Cingolani, R.; Pompa, P.P. SiO 2 nanoparticles biocompatibility and their potential for gene delivery and silencing. *Nanoscale* **2012**, *4*, 486–495.
50. Wheeler, P.A.; Wang, J.; Baker, J.; Mathias, L.J. Synthesis and characterization of covalently functionalized laponite clay. *Chemistry of Materials* **2005**, *17*, 3012–3018.
51. Kuang, G.; Zhang, Q.; He, S.; Liu, Y. Curcumin-loaded PEGylated mesoporous silica nanoparticles for effective photodynamic therapy. *RSC Advances* **2020**, *10*, 24624–24630.
52. Chen, K.; Chang, C.; Liu, Z.; Zhou, Y.; Xu, Q.; Li, C.; Huang, Z.; Xu, H.; Xu, P.; Lu, B. Hyaluronic acid targeted and

pH-responsive nanocarriers based on hollow mesoporous silica nanoparticles for chemo-photodynamic combination therapy. *Colloids and Surfaces B: Biointerfaces* **2020**, *194*, 111166–111174.

53. Lyles, Z.K.; Tarannum, M.; Mena, C.; Inada, N.M.; Bagnato, V.S.; Vivero-Escoto, J.L. Biodegradable Silica-Based Nanoparticles with Improved and Safe Delivery of Protoporphyrin IX for the In Vivo Photodynamic Therapy of Breast Cancer. *Advanced Therapeutics* **2020**, *3*, 2000022–2000038.
54. Ellahioui, Y.; Patra, M.; Mari, C.; Kaabi, R.; Karges, J.; Gasser, G.; Gómez-Ruiz, S. Mesoporous silica nanoparticles functionalised with a photoactive ruthenium(ii) complex: Exploring the formulation of a metal-based photodynamic therapy photosensitiser. *Dalton Transactions* **2019**, *48*, 5940–5951.
55. Figueira, F.; Cavaleiro, J.A.S.; Tomé, J.P.C. Silica nanoparticles functionalized with porphyrins and analogs for biomedical studies. *Journal of Porphyrins and Phthalocyanines* **2011**, *15*, 517–533.
56. Martins Estevão, B.; Miletto, I.; Marchese, L.; Gianotti, E. Optimized Rhodamine B labeled mesoporous silica nanoparticles as fluorescent scaffolds for the immobilization of photosensitizers: a theranostic platform for optical imaging and photodynamic therapy. *Phys. Chem. Chem. Phys.* **2016**, *18*, 9042–9052.
57. Ronzani, F.; Costarramone, N.; Blanc, S.; Benabbou, A.K.; Bechec, M. Le; Pigot, T.; Oelgemöller, M.; Lacombe, S. Visible-light photosensitized oxidation of α-terpinene using novel silica-supported sensitizers: Photooxygenation vs. photodehydrogenation. *Journal of Catalysis* **2013**, *303*, 164–174.
58. Gianotti, E.; Martins Estevão, B.; Cucinotta, F.; Hioka, N.; Rizzi, M.; Renò, F.; Marchese, L. An Efficient Rose Bengal Based Nanoplatform for Photodynamic Therapy. *Chemistry - A European Journal* **2014**, *20*, 10921–10925.
59. Cheng, S.-H.; Lee, C.-H.; Yang, C.-S.; Tseng, F.-G.; Mou, C.-Y.; Lo, L.-W. Mesoporous silica nanoparticles functionalized with an oxygen-sensing probe for cell photodynamic therapy: potential cancer theranostics. *Journal of Materials Chemistry* **2009**, *19*, 1252–1257.
60. Martins Estevão, B.; Cucinotta, F.; Hioka, N.; Cossi, M.; Argeri, M.; Paul, G.; Marchese, L.; Gianotti, E. Rose Bengal incorporated in mesostructured silica nanoparticles: structural characterization, theoretical modeling and singlet oxygen delivery. *Phys. Chem. Chem. Phys.* **2015**, *17*, 26804–26812.
61. Kan, J.L.; Jiang, Y.; Xue, A.; Yu, Y.H.; Wang, Q.; Zhou, Y.; Dong, Y. Bin Surface Decorated Porphyrinic Nanoscale Metal-Organic Framework for Photodynamic Therapy. *Inorganic Chemistry* **2018**, *57*, 5420–5428.
62. Wang, S.; Fan, W.; Kim, G.; Hah, H.J.; Lee, Y.E.K.; Kopelman, R.; Ethirajan, M.; Gupta, A.; Goswami, L.N.; Pera, P.; et al. Novel methods to incorporate photosensitizers into nanocarriers for cancer treatment by photodynamic therapy. *Lasers in Surgery and Medicine* **2011**, *43*, 686–695.
63. Tada, D.B.; Baptista, M.S. Photosensitizing nanoparticles and the modulation of ROS generation. *Frontiers in Chemistry* **2015**, *3*, 1–14.
64. Alexander, W. American society of clinical oncology, 2010 annual meeting and rose bengal: from a wool dye to a cancer therapy. *P & T : a peer-reviewed journal for formulary management* **2010**, *35*, 469–78.
65. Gualdesi, M.S.; Vara, J.; Aiassa, V.; Alvarez Igarzabal, C.I.; Ortiz, C.S. Thionine in the design of new photosensitizers: Bromination and vehiculization in polymeric nanoparticles. *Journal of Molecular Liquids* **2020**, *310*, 113247–113256.
66. Tuite, E.M.; Kelly, J.M. New trends in photobiology. Photochemical interactions of methylene blue and analogues with DNA and other biological substrates. *Journal of Photochemistry and Photobiology, B: Biology* **1993**, *21*, 103–124.
67. Kabanov, V.; Press, D.J.; Huynh, R.P.S.; Shimizu, G.K.H.; Heyne, B. Assessment of encapsulated dyes' distribution in silica nanoparticles and their ability to release useful singlet oxygen. *Chemical Communications* **2018**, *54*, 6320–6323.
68. Liu, J.Y.; Zhou, P.Z.; Ma, J.L.; Jia, X. Trifluoromethyl boron dipyrromethene derivatives as potential photosensitizers for photodynamic therapy. *Molecules* **2018**, *23*, 1–13.
69. Zahraei, M.; Marciello, M.; Lazaro-Carrillo, A.; Villanueva, A.; Herranz, F.; Talelli, M.; Costo, R.; Monshi, A.; Shahbazi-Gahrouei, D.; Amirnasr, M.; et al. Versatile theranostics agents designed by coating ferrite nanoparticles with biocompatible polymers. *Nanotechnology* **2016**, *27*, 255702–255714.

70. Asefa, T.; Tao, Z. Biocompatibility of mesoporous silica nanoparticles. *Chemical Research in Toxicology* **2012**, *25*, 2265–2284.
71. He, Q.; Zhang, J.; Shi, J.; Zhu, Z.; Zhang, L.; Bu, W.; Guo, L.; Chen, Y. The effect of PEGylation of mesoporous silica nanoparticles on nonspecific binding of serum proteins and cellular responses. *Biomaterials* **2010**, *31*, 1085–1092.
72. Suk, J.S.; Xu, Q.; Kim, N.; Hanes, J.; Ensign, L.M. PEGylation as a strategy for improving nanoparticle-based drug and gene delivery. *Advanced Drug Delivery Reviews* **2016**, *99*, 28–51.
73. Manzano, M.; Vallet-Regí, M. Mesoporous Silica Nanoparticles for Drug Delivery. *Advanced Functional Materials* **2020**, *30*, 1902634.
74. Yoo, J.; Park, C.; Yi, G.; Lee, D.; Koo, H. Active Targeting Strategies Using Biological Ligands for Nanoparticle Drug Delivery Systems. *Cancers* **2019**, *11*, 640–653.
75. Fernández, M.; Javaid, F.; Chudasama, V. Advances in targeting the folate receptor in the treatment/imaging of cancers. *Chemical Science* **2018**, *9*, 790–810.
76. Santiago, A.M.; Ribeiro, T.; Rodrigues, A.S.; Ribeiro, B.; Frade, R.F.M.; Baleizão, C.; Farinha, J.P.S. Multifunctional Hybrid Silica Nanoparticles with a Fluorescent Core and Active Targeting Shell for Fluorescence Imaging Biodiagnostic Applications. *European Journal of Inorganic Chemistry* **2015**, *2015*, 4579–4587.
77. Van Dam, G.M.; Themelis, G.; Crane, L.M.A.; Harlaar, N.J.; Pleijhuis, R.G.; Kelder, W.; Sarantopoulos, A.; De Jong, J.S.; Arts, H.J.G.; Van Der Zee, A.G.J.; et al. Intraoperative tumor-specific fluorescence imaging in ovarian cancer by folate receptor-α targeting: First in-human results. *Nature Medicine* **2011**, *17*, 1315–1319.
78. Pérez-Herrero, E.; Fernández-Medarde, A. Advanced targeted therapies in cancer: Drug nanocarriers, the future of chemotherapy. *European Journal of Pharmaceutics and Biopharmaceutics* **2015**, *93*, 52–79.
79. Zwicke, G.L.; Ali Mansoori, G.; Jeffery, C.J. Utilizing the folate receptor for active targeting of cancer nanotherapeutics. *Nano Reviews* **2012**, *3*, 18496–18507.
80. Prieto-Montero, R.; Katsumiti, A.; Cajaraville, M.P.; Lopez Arbeloa, I.; Martinez-Martinez, V. Functionalized Fluorescent Silica Nanoparticles for Bioimaging of Cancer Cells. *Sensors* **2020**, *20*, 5590–5605.
81. Epelde-Elezcano, N.; Prieto-Montero, R.; Martínez-Martínez, V.; Ortiz, M.J.; Prieto-Castañeda, A.; Peña-Cabrera, E.; Belmonte-Vázquez, J.L.; López-Arbeloa, I.; Brown, R.; Lacombe, S. Adapting BODIPYs to singlet oxygen production on silica nanoparticles. *Physical Chemistry Chemical Physics* **2017**, *19*, 13746–13755.
82. Fraix, A.; Blangetti, M.; Guglielmo, S.; Lazzarato, L.; Marino, N.; Cardile, V.; Graziano, A.C.E.; Manet, I.; Fruttero, R.; Gasco, A.; et al. Light-tunable generation of singlet oxygen and nitric oxide with a bichromophoric molecular hybrid: A bimodal approach to killing cancer cells. *ChemMedChem* **2016**, *11*, 1371–1379.
83. Wu, G.; Zeng, F.; Wu, S. A water-soluble and specific BODIPY-based fluorescent probe for hypochlorite detection and cell imaging. *Analytical Methods* **2013**, *5*, 5589–5596.
84. Guo, S.; Zhang, H.; Huang, L.; Guo, Z.; Xiong, G.; Zhao, J. Porous material-immobilized iodo-Bodipy as an efficient photocatalyst for photoredox catalytic organic reaction to prepare pyrrolo[2,1-a]isoquinoline. *Chemical Communications* **2013**, *49*, 8689–8702.
85. Nad, S.; Kumbhakar, M.; Pal, H. Photophysical Properties of Coumarin-152 and Coumarin-481 Dyes:Unusual Behavior in Nonpolar and in Higher Polarity Solvents. *J. Phys. Chem. A* **2003**, 4808–4816.
86. Magde, D.; Brannon, J.H.; Cremers, T.L.; Olmsted, J. Absolute luminescence yield of cresyl violet. A standard for the red. *Journal of Physical Chemistry* **1979**, *83*, 696–699.
87. Vincett, P.S.; Voigt, E.M.; Rieckhoff, K.E. Phosphorescence and Fluorescence of Phthalocyanines. *The Journal of Chemical Physics* **1971**, *55*, 4131–4140.
88. Prieto-Montero, R.; Sola-Llano, R.; Montero, R.; Longarte, A.; Arbeloa, T.; López-Arbeloa, I.; Martínez-Martínez, V.; Lacombe, S. Methylthio BODIPY as a standard triplet photosensitizer for singlet oxygen production: a photophysical study. *Physical Chemistry Chemical Physics* **2019**, *21*, 20403–20414.
89. Mai, W.X.; Meng, H. Mesoporous silica nanoparticles: A multifunctional nano therapeutic system. *Integrative Biology* **2013**, *5*,

19–28.

90. Stöber, W.; Fink, A.; Bohn, E. Controlled growth of monodisperse silica spheres in the micron size range. *Journal of Colloid and Interface Science* **1968**, *26*, 62–69.
91. Arulprakasajothi, M.; Elangovan, K.; Chandrasekhar, U.; Suresh, S. Performance Study of Conical Strip Inserts in Tube Heat. *thermal science* **2018**, *22*, 477–485.
92. Maurel, M.; Montheil, T.; Martin, J.; Chaar, L.; Guzman-Gonzalez, V.; Couvet, M.; Jacquet, T.; Jia, T.; Eymin, B.; Parra, K.; et al. Design of pegylated three ligands silica nanoparticles for multi-receptor targeting. *Nanomaterials* **2021**, *11*, 1–23.
93. Cruz, L.J.; Tacken, P.J.; Fokkink, R.; Figdor, C.G. The influence of PEG chain length and targeting moiety on antibody-mediated delivery of nanoparticle vaccines to human dendritic cells. *Biomaterials* **2011**, *32*, 6791–6803.
94. Chithrani, D.B. Polyethylene Glycol Density and Length Affects Nanoparticle Uptake by Cancer Cells. *Journal of Nanomedicine Research* **2014**, *1*, 1–6.
95. Off, M.K.; Steindal, A.E.; Porojnicu, A.C.; Juzeniene, A.; Vorobey, A.; Johnsson, A.; Moan, J. Ultraviolet photodegradation of folic acid. *Journal of Photochemistry and Photobiology B: Biology* **2005**, *80*, 47–55.
96. Duman, S.; Cakmak, Y.; Kolemen, S.; Akkaya, E.U.; Dede, Y. Heavy atom free singlet oxygen generation: Doubly substituted configurations dominate S 1 states of bis-BODIPYs. *Journal of Organic Chemistry* **2012**, *77*, 4516–4527.
97. Tao, J.; Sun, D.; Sun, L.; Li, Z.; Fu, B.; Liu, J.; Zhang, L.; Wang, S.; Fang, Y.; Xu, H. Tuning the photo-physical properties of BODIPY dyes: Effects of 1, 3, 5, 7- substitution on their optical and electrochemical behaviours. *Dyes and Pigments* **2019**, *168*, 166–174.
98. Gibbs, J.H.; Zhou, Z.; Kessel, D.; Fronczek, F.R.; Pakhomova, S.; Vicente, M.G.H. Synthesis, spectroscopic, and in vitro investigations of 2,6-diiodo-BODIPYs with PDT and bioimaging applications. *Journal of Photochemistry and Photobiology B: Biology* **2015**, *145*, 35–47.
99. Awuah, S.G.; You, Y. Boron dipyrromethene (BODIPY)-based photosensitizers for photodynamic therapy. *RSC Advances* **2012**, *2*, 11169–11183.
100. Agazzi, M.L.; Ballatore, M.B.; Durantini, A.M.; Durantini, E.N.; Tomé, A.C. BODIPYs in antitumoral and antimicrobial photodynamic therapy: An integrating review. *Journal of Photochemistry and Photobiology C: Photochemistry Reviews* **2019**, *40*, 21–48.
101. Lim, S.H.; Thivierge, C.; Nowak-Sliwinska, P.; Han, J.; Van Den Bergh, H.; Wagnières, G.; Burgess, K.; Lee, H.B. In vitro and in vivo photocytotoxicity of boron dipyrromethene derivatives for photodynamic therapy. *Journal of Medicinal Chemistry* **2010**, *53*, 2865–2874.
102. Ventura, B.; Marconi, G.; Bröring, M.; Krüger, R.; Flamigni, L. Bis(BF2)-2,2′-bidipyrrins, a class of BODIPY dyes with new spectroscopic and photophysical properties. *New Journal of Chemistry* **2009**, *33*, 428–438.
103. Epelde-Elezcano, N.; Palao, E.; Manzano, H.; Prieto-Castañeda, A.; Agarrabeitia, A.R.; Tabero, A.; Villanueva, A.; de la Moya, S.; López-Arbeloa, Í.; Martínez-Martínez, V.; et al. Rational Design of Advanced Photosensitizers Based on Orthogonal BODIPY Dimers to Finely Modulate Singlet Oxygen Generation. *Chemistry - A European Journal* **2017**, *23*, 4837–4848.
104. Pang, W.; Zhang, X.; Zhou, J.; Yu, C.; Hao, E.; Jiao, L. Modulating the singlet oxygen generation property of meso–β directly linked BODIPY dimers. *Chemical Communications* **2012**, *48*, 5437–5439.
105. Wu, W.; Cui, X.; Zhao, J. Hetero Bodipy-dimers as heavy atom-free triplet photosensitizers showing a long-lived triplet excited state for triplet–triplet annihilation upconversion. *Chemical Communications* **2013**, *49*, 9009–9012.
106. Bharathiraja, S.; Moorthy, M.S.; Manivasagan, P.; Seo, H.; Lee, K.D.; Oh, J. Chlorin e6 conjugated silica nanoparticles for targeted and effective photodynamic therapy. *Photodiagnosis and Photodynamic Therapy* **2017**, *19*, 212–220.